

Cylindrical Circular and Elliptical, Toroidal Circular and Elliptical Multipoles Fields, Potentials and their Measurement for Accelerator Magnets

Pierre Schnizer* and Egbert Fischer†

GSI Helmholtzzentrum für Schwerionenforschung mbH, Planckstraße 1, 64291 Darmstadt, Germany

Bernhard Schnizer‡

*Institut für theoretische Physik - Computational Physics,
Technische Universität Graz, Petersgasse 16, 8010 Graz, Austria*

(Dated: October 30, 2014)

Recent progress in particle accelerator tracking has shown that the field representation is one of the major limits of the prediction accuracy especially for machines, whose aperture is fully filled by the beam and thus higher the artefacts created by higher order modes have to be thoroughly understood.

The standard tool for field presentation today are cylindrical circular multipoles due to their straight forward correspondence to the Cartesian coordinates. In this paper we extend the standard approach to other coordinate systems, show how these can be measured next to their realisation in measuring the SIS100 Magnets for the FAIR project.

PACS numbers: 41.20.Gz

Keywords: harmonics, magnetic fields, magnetic field measurement

I. INTRODUCTION

Studying the performance of an existing or to be built accelerator requires solid knowledge on the magnetic field quality so that the expected beam behaviour can be calculated. Nowadays the field of each type of magnet can be calculated by numerical codes. But analytic expressions of the portion of the static or quasi-static magnetic field in the gap are needed for beam dynamics calculations. In that part of the gap which is free from conductors or charges the field is a potential field. Therefore expansions of the potential are used comprising particular solutions of the potential equation to describe this field. Their coefficients are obtained by fitting the expansions to the numerical field values produced by the code. Such particular solutions are obtained by solving the potential equation by separation and are called multipoles.

All textbooks related to accelerator physics have been using local Cartesian or cylindrical circular coordinate systems to describe the field in long magnets. (Transverse deviations of the particle from the ideal orbit are followed by the Frenet Serret coordinates.) While this approach is general and has proven to be applicable by experience and manageable with the computing power typically available in the last decade, producing the circular expansion coefficients has shown to be troublesome for practical accelerator magnets, in particular for iron dominated ones, where the height of the gap is considerably smaller than the aperture width. Here the standard approach calculating the multipoles over a circular boundary will not work as $\Delta\Phi = 0$ is not defined everywhere if the

circle is chosen with a radius equal to half the width of the aperture. Similarly data obtained from the boundary of a circle with a radius equal to half the height will represent the field only slightly beyond the measurement radius.

During the R&D phase of the heavy ion synchrotron SIS100 these problems had to be tackled as the beam uses considerable area of the elliptic vacuum chamber. This led to the development of elliptic cylindrical multipoles [1–3].

During the R&D phase the design of the dipole magnets, originally straight 2 T, 4 T/s, 2.65 m long magnets, were changed to curved ones with a radius of curvature of 52.625 m. As the advanced beam dynamics studies required a set of reliable harmonics, a concise solution was required to be able to develop a measurement concept and to extract data for beam dynamics use. The appropriate multipoles were derived using local toroidal coordinates and the technique of R-separation, as these give simpler solutions, as the global toroidal ones (see e.g. [4, 5]), and are easier to interpret [2, 6]. The solution was then further extended to elliptic toroidal multipoles [7].

All these developments were driven by the limitations we found in the standard tool, the cylindrical circular multipoles, and were developed for designing the SIS100 synchrotron, measuring the dipole magnets and predicting the performance of the machine.

This paper is split into the following parts:

1. First the mathematics of the cylindrical circular multipoles is recalled.
2. The different new coordinate systems are described in a way, which always clearly shows their relation to the preceding system next to the properties of the obtained solutions.

* p.schnizer@gsi.de

† e.fischer@gsi.de

‡ bernhard.schnizer@tugraz.at

3. Finally their application is illustrated showing how these multipoles can be measured.

While these developments have been made for SIS100, the solutions obtained are applicable to any problem formulated by the potential equation in the geometries given above.

II. THEORY

A. Plane Circular Multipoles

The circular multipoles are the common workhorse for representing the two-dimensional field in the gap of long straight accelerator magnets. Here just the most important formulas are listed. Details may be found in the papers of [8] and [9].

Circular multipoles are particular regular solutions of the potential equation

$$\Delta\Phi_r = 0 \quad (1)$$

in Cartesian coordinates (x, y) or in polar coordinates ρ, θ with $x = \rho \cos \theta$, $y = \rho \sin \theta$:

$$\Delta\Phi_r = \left(\frac{\partial^2}{\partial x^2} + \frac{\partial^2}{\partial y^2} \right) \Phi_r = 0, \quad (2)$$

$$\Delta\Phi_r = \left(\frac{\partial^2}{\partial r^2} + \frac{1}{r} \frac{\partial}{\partial r} + \frac{\partial^2}{\partial \theta^2} \right) \Phi_r = 0. \quad (3)$$

Any non-negative integer power

$$\begin{aligned} \mathbf{C}_m(\mathbf{z}/R_{Ref})^m &= \mathbf{C}_m [(x + iy)/R_{Ref}]^m \\ &= \mathbf{C}_m (r/R_{Ref})^m e^{im\theta}, \quad m = 0, 1, 2, \dots \end{aligned} \quad (4)$$

is such a complex regular solution of Eqs. (2) or (3). The reference radius R_{Ref} is inserted to render all the solutions dimensionless and of similar magnitude. The complex constants \mathbf{C}_m determine the magnitude and the direction of each multipole. In practice the irrotational and source-free magnetic induction of a single ideal multipole may be written in a concise complex representation as:

$$\begin{aligned} \mathbf{B}(\mathbf{z}) &:= B_y(x, y) + i B_x(x, y) \\ &= \mathbf{C}_m \left(\frac{\mathbf{z}}{R_{Ref}} \right)^{m-1} = \mathbf{C}_m \left(\frac{r}{R_{Ref}} \right)^{m-1} e^{i(m-1)\theta}. \end{aligned} \quad (5)$$

The induction in a real long magnet is a superposition of such multipoles:

$$\mathbf{B}^C(\mathbf{z}) := B_y^C(x, y) + i B_x^C(x, y) = \sum_{m=1}^M \mathbf{C}_m (\mathbf{z}/R_{Ref})^{m-1}. \quad (6)$$

Here the European convention is adopted: $m = 1$ gives a dipole field, $m = 2$ a quadrupole field, a.s.o. M is the number of multipoles used; in theory $M = \infty$, in practice M is about 20.

TABLE I. Cylindric circular multipoles, first terms of the potential and the basis functions.

	$\Phi_r(x, y)$	$B_x(x, y)$	$B_y(x, y)$
normal			
1	$-\frac{y}{R_{Ref}}$	0	1
2	$-\frac{xy}{R_{Ref}^2}$	$\frac{y}{R_{Ref}}$	$\frac{x}{R_{Ref}}$
3	$\frac{y(-3x^2+y^2)}{3R_{Ref}^3}$	$2\frac{xy}{R_{Ref}^2}$	$\frac{x^2-y^2}{R_{Ref}^2}$
4	$\frac{xy(-x^2+y^2)}{R_{Ref}^4}$	$\frac{y(3x^2-y^2)}{R_{Ref}^3}$	$\frac{x(x^2-3y^2)}{R_{Ref}^3}$
skew			
1	$-\frac{x}{R_{Ref}}$	1	0
2	$\frac{-x^2+y^2}{2R_{Ref}^2}$	$\frac{x}{R_{Ref}}$	$-\frac{y}{R_{Ref}}$
3	$\frac{x(-x^2+3y^2)}{3R_{Ref}^3}$	$\frac{x^2-y^2}{R_{Ref}^2}$	$-2\frac{xy}{R_{Ref}^2}$
4	$\frac{-x^4+6x^2y^2-y^4}{4R_{Ref}^4}$	$\frac{x(x^2-3y^2)}{R_{Ref}^3}$	$\frac{y(-3x^2+y^2)}{R_{Ref}^3}$

The two equations above define complex functions having a complex potential:

$$\mathbf{B}^C(\mathbf{z}) = -R_{Ref} d\Phi^C/dz. \quad (7)$$

A simple integration gives:

$$\Phi^C(\mathbf{z}) = - \sum_{m=1}^M \frac{1}{m} \mathbf{C}_m (\mathbf{z}/R_{Ref})^m = - \sum_{m=1}^M \mathbf{C}_m \Phi_m^C(\mathbf{z}). \quad (8)$$

A zero value has been assumed for the integration constant; so $\Phi^C(\mathbf{z} = 0) = 0$.

1. Normal circular multipoles

Assuming real values of the constants $\mathbf{C}_m = B_m$, then taking the imaginary part of the resulting potential $\Phi^C(\mathbf{z})$, Eq. (8) gives the real potential $\Phi^{Cn}(x, y)$. The real components of the magnetic induction can be computed from this real potential:

$$\begin{aligned} (B_x^{Cn}, B_y^{Cn}) &= -R_{Ref} \text{grad}\Phi^{Cn}(x, y) \\ &= -R_{Ref} \left(\frac{\partial}{\partial x}, \frac{\partial}{\partial y} \right) \Phi^{Cn}(x, y). \end{aligned} \quad (9)$$

$$\begin{aligned} \Phi^{Cn} &= - \sum_{m=1}^M B_m \Phi_m^{Cn} \\ &= - \sum_{m=1}^M B_m \frac{1}{m} \text{Im} \left(\frac{\mathbf{z}}{R_{Ref}} \right)^m. \end{aligned} \quad (10)$$

The first terms are listed in Table I. A zero value has been assumed for the integration constant; so $\Phi^{Cn}(\mathbf{z} = 0) = 0$. The normal multipole fields are a vertical induction B_y for $m = 1$: a quadrupole with pole faces normal to the coordinate axes at $x = 0$, $y = 0$ respectively, for $m = 2$; a.s.o. The same field expressions as in Eq. (9) are also found by taking real and imaginary parts of the complex field representation $\mathbf{B}^C(\mathbf{z})$, Eq. (6).

2. Skew circular multipoles

Assuming purely imaginary values of the constants $\mathbf{C}_m = iA_m$, then taking the imaginary part of the resulting potential $\Phi^C(\mathbf{z})$, Eq. (8), gives the real potential $\Phi^{Cs}(x, y)$. The real components of the magnetic induction can be computed from this real potential:

$$\begin{aligned} (B_x^{Cs}, B_y^{Cs}) &= -R_{Ref} \text{grad} \Phi^{Cs}(x, y) \\ &= -R_{Ref} \left(\frac{\partial}{\partial x}, \frac{\partial}{\partial y} \right) \Phi^{Cs}(x, y); \end{aligned} \quad (11)$$

$$\begin{aligned} \Phi^{Cs}(x, y) &= - \sum_{m=1}^M A_m \Phi_m^{Cs} \\ &= - \sum_{m=1}^M A_m \frac{1}{m} \text{Re} \left(\frac{\mathbf{z}}{R_{Ref}} \right)^m. \end{aligned} \quad (12)$$

A zero value has been assumed for the integration constant; so $\Phi^{Cs}(\mathbf{z} = 0) = 0$.

So one gets skew multipoles. This is a purely horizontal magnetic induction B_x for $m = 1$; a quadrupole with pole faces normal to the bisectors of the coordinate axes for $m = 2$; a.s.o. The same field expressions as in Eq. (11) are also found by taking real and imaginary parts of the complex field representation $\mathbf{B}^C(\mathbf{z})$, Eq. (6).

B. Elliptic multipoles

1. Elliptic coordinates

Elliptic coordinates are superior to circular coordinates in gaps of elliptic cross section, as typically used as beam aperture when iron dominated magnets are used for guiding the beam. An ellipse as reference curve covers a larger area than an inscribed circle. The reference ellipse is defined by its semi-axes a and b giving the eccentricity e . Plane elliptic coordinates η, ψ may be introduced by a conformal mapping:

$$\mathbf{z} := x + iy = e \cosh \mathbf{w}, \quad \mathbf{w} := \eta + i\psi; \quad (13)$$

$$\mathbf{w} = \text{Arcosh}(\mathbf{z}/e), \quad \eta_0 = \text{ArTanh}(b/a) \quad (14)$$

η_0 is the value of the quasi-radial variable η corresponding to the reference ellipse. Taking the real and the imaginary part of Eq. (13) gives a real vector $\mathbf{r} = (x, y)$. Computing the tangent vectors \mathbf{r}_η and \mathbf{r}_ψ , normalising and generalising them gives formulas for transforming components of the same vector \mathbf{a} between the Cartesian and the elliptic system:

$$a_\eta = \sinh \eta \cos \psi a_x/h_t + \cosh \eta \sin \psi a_y/h_t, \quad (15)$$

$$a_\psi = -\cosh \eta \sin \psi a_x/h_t + \sinh \eta \cos \psi a_y/h_t;$$

$$h_t = e \sqrt{\cosh^2 \eta \sin^2 \psi + \sinh^2 \eta \cos^2 \psi} = \quad (16)$$

$$= e \sqrt{\cosh^2 \eta - \cos^2 \psi} = e \sqrt{\sinh^2 \eta + \sin^2 \psi}$$

The arc element is:

$$ds^2 = dx^2 + dy^2 = h_t^2 (d\eta^2 + d\psi^2). \quad (17)$$

2. Elliptic multipole field expansions for Cartesian components depending on elliptic coordinates

Solutions of the potential equation, so multipoles in elliptic coordinates were introduced and discussed at length in [3]. The first basis terms are given in Table II. Here only some important formulas are quoted from this source and some new results will be given. Analogous to Eq. (6) we define a complex field representation depending on the elliptic coordinates η, ψ through $\mathbf{w} = \eta + i\psi$ as:

$$\mathbf{B}^{Ce}(\mathbf{w}) = B_y^{Ce}(\eta, \psi) + iB_x^{Ce}(\eta, \psi) \quad (18)$$

$$\begin{aligned} &:= \frac{\mathbf{E}_1}{2} + \sum_{k=2}^M \mathbf{E}_k \frac{\cosh((k-1)(\eta + i\psi))}{\cosh((k-1)\eta_0)} \\ &:= -d\Xi^{Ce}/d\mathbf{w} \end{aligned} \quad (19)$$

$$= \sum_{k=1}^M \mathbf{E}_k \frac{1}{1 + \delta_{k1}} \frac{\cosh((k-1)\mathbf{w})}{\cosh((k-1)\eta_0)}$$

$\cosh(= \mathbf{C}_m(\eta + i\psi))$ is a regular solution of the potential equation in elliptic coordinates:

$$\Delta \Phi_r^e = \frac{1}{h_t^2} \left[\frac{\partial^2}{\partial \eta^2} + \frac{\partial^2}{\partial \psi^2} \right] \Phi_r^e = 0. \quad (20)$$

TABLE II. The basis functions of the cylindric elliptic multipoles.

	Φ_r^e	$B_x(x, y)$	$B_y(x, y)$
normal			
1	$-\frac{\psi}{2}$	0	$\frac{1}{2}$
2	$-\cosh(\eta) \sin(\psi)$	$\sin(\psi) \sinh(\eta)$	$\cos(\psi) \cosh(\eta)$
3	$-\frac{1}{2} \cosh(2\eta) \sin(2\psi)$	$\sin(2\psi) \sinh(2\eta)$	$\cos(2\psi) \cosh(2\eta)$
4	$-\frac{1}{3} \cosh(3\eta) \sin(3\psi)$	$\sin(3\psi) \sinh(3\eta)$	$\cos(3\psi) \cosh(3\eta)$
skew			
1	$-\frac{\eta}{2}$	$\frac{1}{2}$	0
2	$-\sinh(\eta) \cos(\psi)$	$\cos(\psi) \cosh(\eta)$	$-\sin(\psi) \sinh(\eta)$
3	$-\frac{1}{2} \sinh(2\eta) \cos(2\psi)$	$\cos(2\psi) \cosh(2\eta)$	$-\sin(2\psi) \sinh(2\eta)$
4	$-\frac{1}{3} \sinh(3\eta) \cos(3\psi)$	$\cos(3\psi) \cosh(3\eta)$	$-\sin(3\psi) \sinh(3\eta)$

To relate the elliptic multipoles to the circular ones we use the following formula ([10], Eq. 1.331.4)

$$\cosh(\nu \mathbf{w}) = 2^{(\nu-1)} \cosh^\nu \mathbf{w} + \sum_{\mu=1}^{[\nu/2]} (-1)^\mu \frac{\nu}{\mu} \binom{\nu-\mu-1}{\mu-1} 2^{(\nu-2\mu-1)} \cosh^{\nu-2\mu} \mathbf{w} \quad (21)$$

$$= 2^{(\nu-1)} \left(\frac{R_{Ref}}{e} \frac{\mathbf{z}}{R_{Ref}} \right)^\nu + \sum_{\mu=1}^{[\nu/2]} (-1)^\mu \frac{\nu}{\mu} \binom{\nu-\mu-1}{\mu-1} 2^{(\nu-2\mu-1)} \left(\frac{R_{Ref}}{e} \frac{\mathbf{z}}{R_{Ref}} \right)^{\nu-2\mu} \quad (22)$$

$[\nu/2]$ is the largest integer equal to or just below $\nu/2$. The equation above shows that $\mathbf{B}^{Ce}(\mathbf{w})$ is again a linear superposition of plane circular multipoles Eq. (6). But the coefficients of this new series may be computed from data given along the reference ellipse. These data contain more accurate information on higher multipoles. Practical applications show that this new series converges faster and less aleatory [3]. Even when working with circular multipoles in an elliptic aperture it is advantageous to use expansion coefficients \mathbf{C}_m computed from the elliptic coefficients \mathbf{E}_k :

$$\mathbf{C}_m = \left(\frac{R_{Ref}}{e} \right)^{m-1} \sum_{k=1}^M \mathbf{E}_k \frac{(1+\delta_{k1})^{-1}}{\cosh((k-1)\eta_0)} t_{k-1,m-1}. \quad (23)$$

The elements of the real transformation matrix, t_{ms} , have been derived in [3] by a complex integration and Cauchy's residue theorem. An equivalent simpler formula found by rewriting Eq. (21) as

$$\cosh(k\mathbf{w}) = \sum_{\nu=0}^k t_{k\nu} \cosh^\nu w, \quad k = 0, 1, \dots, n. \quad (24)$$

is given here:

$$t_{k\nu} = \begin{cases} 0 & \text{if } k+\nu = \text{odd} \vee k < \nu, \\ 1 & \text{if } k = \nu = 0, \\ 2^{k-1} & \text{if } k = \nu \geq 1, \\ t_{k\nu}^{k>\nu} & \text{if } k-\nu = \text{even} \wedge k > \nu. \end{cases} \quad (25)$$

$$t_{k\nu}^{k>\nu} = \frac{k 2^\nu (-1)^{(k+3\nu)/2} \binom{\frac{k+\nu}{2}-1}{\frac{k-\nu}{2}-1}}{k-\nu} \quad (26)$$

$(t_{k\nu})$ is a lower triangular matrix with a nonzero main diagonal. An even more concise formula due to [11]

$$t_{k\nu} = \text{Coefficient}[T_k(w), w^\nu] \quad (27)$$

uses Chebyshev polynomials defined by:

$$T_k(w) = \cos(k \arccos(w)), \quad -1 \leq w \leq 1; \quad (28)$$

$$= \cosh(k \text{Arcosh}(w)), \quad 1 \leq w < \infty. \quad (29)$$

The complex regular function given in Eq. (19) may be integrated w.r.t. \mathbf{w} to give the auxiliary function $\Xi^{Ce}(\mathbf{w})$ belonging to Eq. (19):

$$\Xi^{Ce}(\mathbf{w}) = -\frac{\mathbf{E}_1}{2} \mathbf{w} - \sum_{k=2}^M \frac{1}{k-1} \mathbf{E}_k \frac{\sinh((k-1)\mathbf{w})}{\cosh((k-1)\eta_0)}. \quad (30)$$

A zero value has been assumed for the integration constant; so $\Xi^{Ce}(\mathbf{w} = 0) = 0$. $\Xi^{Ce}(\mathbf{w})$ is not a single-valued potential. One may derive the Cartesian components of the magnetic induction by the derivatives given in Eqs. ((32)) and ((35)). But it is not the operator grad of the elliptic coordinates, which transforms $\Xi^{Ce}(\mathbf{w})$ into the magnetic induction !

3. Normal multipole expansions for Cartesian components

Assuming real values for the coefficients, $\mathbf{E}_k = E_k^n$, and taking real and imaginary parts of the resulting equation (18) we get the magnetic induction of normal multipoles:

$$B_y^{Cen}(\eta, \psi) = \frac{E_1^n}{2} + \sum_{k=2}^M E_k^n \frac{\cosh((k-1)\eta) \cos((k-1)\psi)}{\cosh((k-1)\eta_0)}, \quad (31)$$

$$B_x^{Cen}(\eta, \psi) = \sum_{k=2}^M E_k^n \frac{\sinh((k-1)\eta) \sin((k-1)\psi)}{\cosh((k-1)\eta_0)}.$$

The corresponding real auxiliary function may be obtained from these formulas by

$$(B_x^{Cen}(\eta, \psi), B_y^{Cen}(\eta, \psi)) = -\left(\frac{\partial}{\partial \eta}, \frac{\partial}{\partial \psi} \right) \Xi^{Cen}(\eta, \psi) \quad (32)$$

or from the imaginary part of $\Xi^e(\mathbf{w})$, [Eq. (30)]:

$$\Xi^{Cen}(\eta, \psi) = -\frac{E_1^n}{2} \psi - \sum_{k=2}^M \frac{1}{k-1} E_k^n \frac{\cosh((k-1)\eta) \sin((k-1)\psi)}{\cosh((k-1)\eta_0)}. \quad (33)$$

4. Skew multipole expansions for Cartesian components

Assuming imaginary values for the coefficients, $\mathbf{E}_k = \mathbf{i}E_k^s$, and taking real and imaginary parts of the resulting equation (18) we get the magnetic induction of skew

multipoles:

$$B_y^{Ces}(\eta, \psi) = - \sum_{k=2}^M E_k^s \frac{\sinh((k-1)\eta) \sin((k-1)\psi)}{\cosh((k-1)\eta_0)}, \quad (34)$$

$$B_x^{Ces}(\eta, \psi) = \frac{E_1^s}{2} + \sum_{k=2}^M E_k^s \frac{\cosh((k-1)\eta) \cos((k-1)\psi)}{\cosh((k-1)\eta_0)}.$$

The corresponding real auxiliary function may be obtained from these formulas by

$$(B_x^{Ces} \eta, \psi), B_y^{Ces}(\eta, \psi)) = - \left(\frac{\partial}{\partial \eta}, \frac{\partial}{\partial \psi} \right) \Xi^{Ces}(\eta, \psi) \quad (35)$$

or from the real part of $\Xi^{Ce}(\mathbf{w})$ (after $\mathbf{E}_k = iE_k^s$ has been inserted !), [Eq. (30)]:

$$\Xi^{Ces}(\eta, \psi) = - \frac{E_1^s}{2} \eta - \sum_{k=2}^M \frac{1}{k-1} E_k^s \frac{\sinh((k-1)\eta) \cos((k-1)\psi)}{\cosh((k-1)\eta_0)}. \quad (36)$$

5. Elliptic multipole field expansions for elliptic components

The field expansions above were for Cartesian components which depend on elliptic coordinates. These are the quantities used in the fits and the evaluations. For applications, the elliptic components are now derived according to the rules of vector analysis in curvilinear coordinates. For that the Cartesian components may be transformed to components B_η, B_ψ by Eq. (15). The corresponding potential may be found with the help of

$$\mathbf{B}^e = -\text{grad}\Phi^e, \quad (B_\eta, B_\psi) = - \frac{1}{h_t} \left(\frac{\partial \Phi^e}{\partial \eta}, \frac{\partial \Phi^e}{\partial \psi} \right). \quad (37)$$

a. Normal multipoles We define new expansion coefficients

$$\bar{E}_k^n = E_k^n / \cosh(k\eta_0) \quad (38)$$

in Eqs. (31) to get simpler expressions. With these and with the transformations Eqs. (15) we get:

$$B_\eta^{en}(\eta, \psi) = \frac{1}{2h_t} \left[\bar{E}_1^n \cosh \eta \sin \psi + \bar{E}_2^n \cosh(2\eta) \sin(2\psi) + \sum_{k=2}^{M-1} \bar{E}_{k+1}^n \left[\cosh[(k+1)\eta] \sin[(k+1)\psi] - \cosh[(k-1)\eta] \sin[(k-1)\psi] \right] \right] \\ = - \frac{1}{h_t} \frac{\partial \Phi^{en}}{\partial \eta} \quad (39)$$

$$B_\psi^{en}(\eta, \psi) = \frac{1}{2h_t} \left[\bar{E}_1^n \sinh \eta \cos \psi + \bar{E}_2^n \sinh(2\eta) \cos(2\psi) + \sum_{k=2}^{M-1} \bar{E}_k^n + 1^n \left[\sinh[(k+1)\eta] \cos[(k+1)\psi] - \sinh[(k-1)\eta] \cos[(k-1)\psi] \right] \right] \\ = - \frac{1}{h_t} \frac{\partial \Phi^{en}}{\partial \psi}. \quad (40)$$

$$\Phi^{en}(\eta, \psi) = - \frac{1}{2} \left[\bar{E}_1^n \sinh \eta \sin \psi + \bar{E}_2^n \frac{1}{2} \sinh(2\eta) \sin(2\psi) + \sum_{k=2}^{M-1} \bar{E}_{k+1}^n \left[\frac{\sinh[(k+1)\eta] \sin[(k+1)\psi]}{k+1} - \frac{\sinh[(k-1)\eta] \sin[(k-1)\psi]}{k-1} \right] \right] \quad (41)$$

b. Skew multipoles From Eq. (34), which were obtained with $\mathbf{E}_k = iE_k^s$, with

$$\bar{E}_k^s = E_k^s / \cosh(k\eta_0) \quad (42)$$

and with Eq. (15) we get:

$$B_{\eta}^{es}(\eta, \psi) = \frac{1}{2h_t} \left[\bar{E}_1^s \sinh \eta \cos \psi + \bar{E}_2^s \sinh(2\eta) \cos(2\psi) + \right. \quad (43)$$

$$\left. + \sum_{k=2}^{M-1} \bar{E}_{k+1}^s \left[\sinh[(k+1)\eta] \cos[(k+1)\psi] - \sinh[(k-1)\eta] \cos[(k-1)\psi] \right] \right]$$

$$= -\frac{1}{h_t} \frac{\partial \Phi^{es}}{\partial \eta},$$

$$B_{\psi}^{es}(\eta, \psi) = -\frac{1}{2h_t} \left[\bar{E}_1^s \cosh \eta \sin \psi + \bar{E}_2^s \cosh(2\eta) \sin(2\psi) + \right. \quad (44)$$

$$\left. + \sum_{k=2}^{M-1} \bar{E}_{k+1}^s \left[\cosh[(k+1)\eta] \sin[(k+1)\psi] - \cosh[(k-1)\eta] \sin[(k-1)\psi] \right] \right]$$

$$= -\frac{1}{h_t} \frac{\partial \Phi^{es}}{\partial \psi}.$$

$$\Phi^{es}(\eta, \psi) = -\frac{1}{2} \left[\bar{E}_1^s \cosh \eta \cos \psi + \bar{E}_2^s \frac{1}{2} \cosh(2\eta) \cos(2\psi) + \right. \quad (45)$$

$$\left. + \sum_{k=2}^{M-1} \bar{E}_{k+1}^s \left[\frac{\cosh[(k+1)\eta] \cos[(k+1)\psi]}{k+1} - \frac{\cosh[(k-1)\eta] \cos[(k-1)\psi]}{k-1} \right] \right].$$

6. Complex potential for normal and skew elliptic multipoles

These series may be combined into one complex series for $B_{\mathbf{w}}^e = B_{\psi}^e + iB_{\eta}^e$. The resulting series may be integrated to give a series for the complex potential:

$$\Phi^e(\mathbf{w}) = -\frac{i}{2} \left[\mathbf{E}_1 \cosh \mathbf{w} + \frac{1}{2} \mathbf{E}_2 \cosh(2\mathbf{w}) + \right. \quad (46)$$

$$\left. + \sum_{k=2}^{M-1} \mathbf{E}_{k+1} \left(\frac{1}{k+1} \cosh[(k+1)\mathbf{w}] - \frac{1}{k-1} \cosh[(k-1)\mathbf{w}] \right) \right].$$

C. Toroidal Multipoles

Toroidal multipole are useful for representing the potential and field in the gap of curved magnets. Up to now, plane circular multipoles have been used to represent these quantities in most cases. But the toroidal multipoles are better adapted to the geometry. Toroidal coordinates (see e.g.[4], Fig.4.4) have an infinite set of nested tori as one set of coordinate surfaces. In these coordinates the potential can be solved exactly by R-separation. An example of this has been given by [12], [5].

Local toroidal coordinates have also an infinite set of nested tori as one set of coordinate surfaces. In these coordinates the potential equation can be solved by approximate R-separation for slender rings. But these so-

lutions are nearer to the plane circular multipoles than the particular solutions of the potential equation in the standard torus coordinates. Since the condition of "slenderness" is met in most practical cases we prefer to use the local toroidal coordinates. In addition this approach can be generalised to slender rings with elliptical cross section.

The toroidal circular multipoles are a complete set of solutions as are the plane circular multipoles. So each of these systems may be employed to expand the potential and the field in the gap of a magnet. However, In a curved magnet the toroidal multipoles give a more accurate solution of the potential equation than the plane circular multipoles.

1. Circular toroidal multipoles

a. Circular local toroidal coordinates These coordinates start from a system of plane polar coordinates r, θ with $x = r \cos \theta$, $y = r \sin \theta$. At first this system is standing in a three-dimensional space X, Y, Z such that the x - and the X - and the y - and the Z -axis are the same. Then the polar system is shifted by R_c along the X -axis. Finally, the shifted system is rotated by an angle ϕ around the original Z -axis. The circles of the shifted polar coordinate system give tori, all having the same centre circle $\sqrt{X^2 + Y^2} = R_c$, $Z = 0$ (see also Fig. 1, [6, 13, 14]). The smaller radius of the torus segment, R_{Ref} , must be smaller than the curvature radius R_c . The coordinates can only be used in the full interior of the reference torus : $\sqrt{x^2 + y^2} \leq R_{Ref} < R_c$.

It is convenient to use a dimensionless quasi-radius $\rho = r/R_{Ref}$. Then the local torus coordinates $R_{Ref}\rho, \theta, \phi$ are defined as:

$$X = R_c h \cos \phi, \quad (47)$$

$$Y = R_c h \sin \phi, \quad (48)$$

$$Z = R_{Ref} \sin \theta; \quad (49)$$

$$h = 1 + \varepsilon \rho \cos \theta. \quad (50)$$

$$0 \leq \varepsilon := R_{Ref}/R_c < 1 \quad (51)$$

is called the inverse aspect ratio. It is smaller than unity; in most accelerators even much smaller. $0 \leq \rho \leq 1$ is denoted as the dimensionless quasi-radius; $-\pi \leq \theta \leq \pi$ as the poloidal angle; $-\phi_0 \leq \phi \leq \phi_0$ as the toroidal (= azimuthal) angle.

b. Circular local toroidal multipoles Here only potentials, so fields, are considered, which are toroidally uniform; thus these quantities are the same in every cross section $\phi = \text{const.}$; they do not depend on the toroidal coordinate ϕ , depend only on the dimensionless quasi-radius ρ and on the poloidal coordinate θ . The corresponding potential is a solution of the following potential equation (some unessential constant factors have been omitted):

$$\Delta \Psi = \quad (52)$$

$$\left[\frac{\partial^2}{\partial \rho^2} + \frac{1}{\rho} \frac{\partial}{\partial \rho} + \frac{1}{\rho^2} \frac{\partial^2}{\partial \theta^2} + \frac{\varepsilon}{h} \left(\cos \theta \frac{\partial}{\partial \rho} - \sin \theta \frac{1}{\rho} \frac{\partial}{\partial \theta} \right) \right] \Psi = 0$$

$$\frac{1}{\sqrt{h}} \left[\frac{\partial^2}{\partial \rho^2} + \frac{1}{\rho} \frac{\partial}{\partial \rho} + \frac{1}{\rho^2} \frac{\partial^2}{\partial \theta^2} + \frac{\varepsilon^2}{h^2} \right] (\sqrt{h} \Psi) = 0. \quad (53)$$

In going to the last equation the dependent variable Ψ has been replaced with $\sqrt{h}\Psi$; this substitution entails the change of the perturbation from a power series in ε starting with a term linear in ε into a new one starting with a quadratic term:

$$\frac{\varepsilon^2}{h^2} = \varepsilon^2 (1 + \varepsilon \rho \cos \theta)^{-2} = \varepsilon^2 (1 - 2\varepsilon \rho \cos \theta + \dots). \quad (54)$$

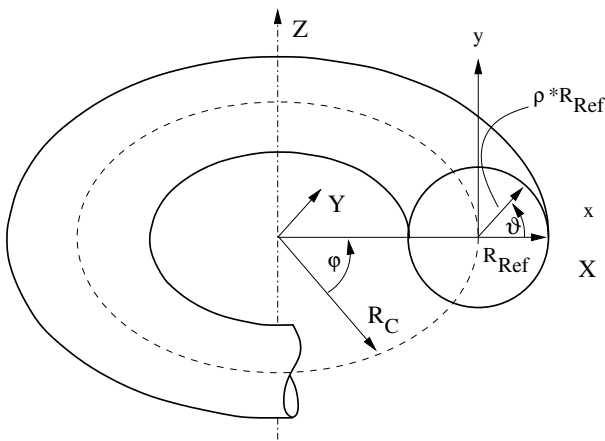


FIG. 1. Relative local toroidal coordinates ρ, θ, ϕ . Graphic courtesy of B. Seiwald [15].

These two interrelated changes are the essence of the R-separation. In the local torus coordinates the term $1/h$ or $1/h^2$ prevents the separation of variables. But dropping ε^2/h^2 or approximating $h^2 \approx 1$ in Eq. (53) both give separable equations. We call this **Approximate R-separation**.

When ε^2/h^2 is dropped in Eq. (53) the resulting differential operator is that of the potential equation in polar coordinates ρ, θ . With a solution of the latter, $\Phi(\rho, \theta)$, we get an approximate solution of the former which is accurate to the first order in ε :

$$\Psi(\rho, \theta) = (1 + \varepsilon \rho \cos \theta)^{-1/2} \Phi(\rho, \theta) + O(\varepsilon^2) \quad (55)$$

$$= \left(1 - \frac{1}{2} \varepsilon \rho \cos \theta\right) \Phi(\rho, \theta) + O(\varepsilon^2).$$

Identifying $\Phi(\rho, \theta)$ with $\Phi_m = \rho^m e^{im\theta}$, $m = 0, 1, 2, \dots$ we get:

$$\Psi_m = h^{-1/2} \rho^m e^{im\theta} \quad (56)$$

$$\approx \rho^m e^{im\theta} \left(1 - \frac{\varepsilon}{4} \rho (e^{i\theta} + e^{-i\theta})\right)$$

$$= \rho^m e^{im\theta} - \frac{\varepsilon}{4} \rho^{m+1} (e^{i(m+1)\theta} + e^{i(m-1)\theta}).$$

In the first order approximation the curvature term adds two terms: $\rho^{m+1} e^{i(m+1)\theta}$ is again a solution of the Laplacian in polar coordinates. At the contrary, the last term alone, i.e. $\rho^{m+1} e^{i(m-1)\theta}$, is not a solution of that operator. Inserting Ψ_m , Eq. (55), into Eq. (52) gives $\Delta \Psi_m = 0 + O(\varepsilon^2)$. So it is verified that Ψ_m is an approximate solution of the potential equation in local toroidal coordinates.

Here it is convenient to define local Cartesian coordinates x, y in the cross section $\phi = \text{const.}$:

$$x = R_{Ref} \rho \cos \theta, \quad y = R_{Ref} \rho \sin \theta; \quad \mathbf{z} = x + iy. \quad (57)$$

and to transform Ψ_m accordingly:

$$\Psi_m = -\frac{1}{m} \left\{ \underbrace{\left(\frac{\mathbf{z}}{R_{Ref}} \right)^{|m|}}_{T_0} - \underbrace{\frac{\varepsilon}{4} \left[\left(\frac{\mathbf{z}}{R_{Ref}} \right)^{|m|+1} + \frac{|\mathbf{z}|^2}{R_{Ref}^2} \left(\frac{\mathbf{z}}{R_{Ref}} \right)^{|m|-1} \right]}_{T_1 + T_2} \right\}. \quad (58)$$

The presence of $|\mathbf{z}|^2$ indicates that Ψ_m is not a complex analytic function of \mathbf{z} . These local Cartesian coordinates correspond to the Cartesian coordinates used for Plane Circular Multipoles in section II A. Multiplying $\Phi^C(x, y)$ by

$$h^{-1/2} = (1 + \varepsilon x/R_{Ref})^{-1/2} \approx 1 - \frac{1}{2} \varepsilon \frac{x}{R_{Ref}} + O(\varepsilon^2);$$

$$S := 1 - \frac{1}{2} \varepsilon \frac{x}{R_{Ref}}$$

gives the wanted approximate solution $\Psi(x, y)$ of the potential equation in local toroidal coordinates. In particular, by this multiplication Φ^{Cn} [Eq. (10)], or Φ^{Cs}

[Eq. (12)], will be transformed to normal or skew potentials $\Psi^{Cn}(\rho, \theta)$ or $\Psi^{Cs}(\rho, \theta)$ for curved magnets:

$$\begin{aligned}\Psi_m^{C\alpha}(x, y) &= S\Phi_m^{C\alpha}(x, y) \\ &= \Phi_m^{C\alpha}(x, y) - \frac{1}{2}\varepsilon \frac{x}{R_{Ref}}\Phi_m^{C\alpha}(x, y); \quad \alpha = n, s\end{aligned}\quad (59)$$

are the normal and the skew toroidal multipoles accurate to the first order in ε .

The potentials Φ^{Cn} [Eq. (10)] or Φ^{Cs} [Eq. (12)] could contain a constant term C_0 , which is not included in the aforementioned equations. Such a constant does not give a contribution to the magnetic induction in the cylindrical case. However, in Eq. (59) it would lead to a non-vanishing toroidal function

$$\Psi_0^{C\alpha}(x, y) = S C_0 = C_0 - \frac{1}{2}\varepsilon \frac{x}{R_{Ref}} C_0.$$

There is a good reason for dropping such a basis function: There is a one-to-one correspondence between the cylindrical and the toroidal basis functions, so between the elements of the two sets of basis functions. The former set is complete, so is the new one. The reference volume of the first set is a straight finite cylinder. The second reference volume is a segment of a torus, which may be obtained from the first one by simple bending it. This operation does not change the topology of the volume. Only a real change of the topological connectivities would provoke the need for additional basis functions.

Vectorial basis functions are needed for expanding the magnetic field. These are obtained by taking the gradients of the potentials

$$\begin{aligned}\vec{T}_m^{C\alpha}(x, y) &= -\nabla\Psi_m^{C\alpha}(x, y) \\ &= -\nabla\Phi_m^{C\alpha}(x, y) + \frac{1}{2}\varepsilon \nabla\left(\frac{x}{R_{Ref}}\Phi_m^{C\alpha}(x, y)\right), \alpha = n, s; \\ &= \left(\begin{array}{c} -\frac{\partial\Phi_m^{C\alpha}(x, y)}{\partial x} + \frac{1}{2}\varepsilon \frac{x}{R_{Ref}}\frac{\partial\Phi_m^{C\alpha}(x, y)}{\partial x} + \frac{1}{2}\varepsilon \frac{1}{R_{Ref}}\Phi_m^{C\alpha}(x, y) \\ -\frac{\partial\Phi_m^{C\alpha}(x, y)}{\partial y} + \frac{1}{2}\varepsilon \frac{x}{R_{Ref}}\frac{\partial\Phi_m^{C\alpha}(x, y)}{\partial y} \end{array}\right),\end{aligned}\quad (60)$$

substituting Φ^{Cn} [Eq. (10)] or Φ^{Cs} [Eq. (12)] for $\Phi^{C\alpha}$. The vector basis functions $\vec{T}_m^{(n)}$ for the normal components B_m are then obtained using Φ^{Cn} and vector basis functions $\vec{T}_m^{(s)}$ for the skew components A_m using Φ^{Cs} .

Any magnetic induction may then expanded in the following way:

$$\vec{B}(x, y) = \sum_{m=1}^M \left[B_m \vec{T}_m^{(n)}(x, y) + A_m \vec{T}_m^{(s)}(x, y) \right]. \quad (61)$$

A complex presentation of the field allows obtaining a closed expression for the magnetic field introducing basis functions $\tilde{\mathbf{T}}_m^{(n)}$, $\tilde{\mathbf{T}}_m^{(s)}$ which fulfil

$$\mathbf{B}(\mathbf{z}) = \sum_{m=1}^M \left[B_m \tilde{\mathbf{T}}_m^{(n)}(\mathbf{z}) + iA_m \tilde{\mathbf{T}}_m^{(s)}(\mathbf{z}) \right]. \quad (62)$$

Comparing Eq. (61) to Eq. (62) one can see that $\tilde{\mathbf{T}}_m^{(n)}$ and $\tilde{\mathbf{T}}_m^{(s)}$ are related to $\vec{T}_m^{(n)}$, $\vec{T}_m^{(s)}$ by

$$\vec{T}_m^{(n)}(x, y) := \text{Re} \left(\tilde{\mathbf{T}}_m^{(n)}(\mathbf{z}) \right) \vec{i}_y + \text{Im} \left(\tilde{\mathbf{T}}_m^{(n)}(\mathbf{z}) \right) \vec{i}_x, \quad (63)$$

$$\vec{T}_m^{(s)}(x, y) := \text{Re} \left(i\tilde{\mathbf{T}}_m^{(s)}(\mathbf{z}) \right) \vec{i}_y + \text{Im} \left(i\tilde{\mathbf{T}}_m^{(s)}(\mathbf{z}) \right) \vec{i}_x. \quad (64)$$

or expressing the complex functions by $\tilde{\mathbf{T}}_m^{(n)}$ and $\tilde{\mathbf{T}}_m^{(s)}$

$$\begin{aligned}\tilde{\mathbf{T}}_m^{(n)}(\mathbf{z}) &= \left(\vec{T}_m^{(n)}(\text{Re}(\mathbf{z}), \text{Im}(\mathbf{z})) \cdot \vec{i}_y \right) \\ &\quad + \left(\vec{T}_m^{(n)}(\text{Re}(\mathbf{z}), \text{Im}(\mathbf{z})) \cdot \vec{i}_x \right) i\end{aligned}\quad (65)$$

$$\begin{aligned}\tilde{\mathbf{T}}_m^{(s)}(\mathbf{z}) &= \left(\vec{T}_m^{(s)}(\text{Re}(\mathbf{z}), \text{Im}(\mathbf{z})) \cdot \vec{i}_y \right) \\ &\quad + \left(\vec{T}_m^{(s)}(\text{Re}(\mathbf{z}), \text{Im}(\mathbf{z})) \cdot \vec{i}_x \right) i\end{aligned}\quad (66)$$

Cylindric circular multipoles are only satisfying the potential equations if $m > 0$ (see e.g. [8]). The same requirement is now imposed on m here as otherwise the aforementioned condition will not be fulfilled for $\varepsilon = 0$. Therefore it is assumed that $m > 0$ holds also for the toroidal circular multipoles. Two methods can now be used to derive these complex functions, both with their merits. The first method uses the fact that the cylindric circular multipoles and their potential can be expressed by the forms given in Eq. (9) and Eq. (10) for the normal multipoles and by Eq. (11) and Eq. (12) for the skew ones. Inserting these expressions in Eq. (60) one obtains for the normal components

$$\vec{T}_m^{(n)}(x, y) = \left(\begin{array}{cc} \text{Im}(\mathbf{B}^C) & -\frac{1}{2}\varepsilon \frac{x}{R_{Ref}} \text{Im}(\mathbf{B}^C) \\ \text{Re}(\mathbf{B}^C) & -\frac{1}{2}\varepsilon \frac{x}{R_{Ref}} \text{Re}(\mathbf{B}^C) \end{array} - \frac{1}{2}\varepsilon \frac{1}{R_{Ref}} \text{Im}(\Phi^{Cn}) \right) = \left(\begin{array}{c} \text{Im} \left[\tilde{\mathbf{T}}_m^{(n)} \right] \\ \text{Re} \left[\tilde{\mathbf{T}}_m^{(n)} \right] \end{array} \right) \quad (67)$$

and for the skew components

$$\vec{T}_m^{(s)}(x, y) = \left(\begin{array}{cc} \text{Im}(i\mathbf{B}^C) & -\frac{1}{2}\varepsilon \frac{x}{R_{Ref}} \text{Im}(i\mathbf{B}^C) \\ \text{Re}(i\mathbf{B}^C) & -\frac{1}{2}\varepsilon \frac{x}{R_{Ref}} \text{Re}(i\mathbf{B}^C) \end{array} - \frac{1}{2}\varepsilon \frac{1}{R_{Ref}} \text{Im}(i\Phi^{Cs}) \right) = \left(\begin{array}{c} \text{Im} \left[i\tilde{\mathbf{T}}_m^{(s)} \right] \\ \text{Re} \left[i\tilde{\mathbf{T}}_m^{(s)} \right] \end{array} \right). \quad (68)$$

These can now be combined to complex ones. Using

$$\text{Im}(\Phi^{\text{Cn}}) = \frac{1}{n} \text{Im}\left(\frac{\mathbf{z}}{R_{\text{Ref}}}\mathbf{B}^{\text{C}}\right) \quad \text{Im}(\mathbf{i}\Phi^{\text{Cn}}) = \frac{1}{n} \text{Im}\left(\mathbf{i}\frac{\mathbf{z}}{R_{\text{Ref}}}\mathbf{B}^{\text{C}}\right) \quad (69)$$

one obtains

$$\begin{pmatrix} \tilde{\tilde{\mathbf{T}}}_{\mathbf{m}}^{(\text{n})}(\mathbf{z}) \\ \tilde{\tilde{\mathbf{T}}}_{\mathbf{m}}^{(\text{s})}(\mathbf{z}) \end{pmatrix} = \left(\frac{\mathbf{z}}{R_{\text{Ref}}}\right)^{n-1} \left(1 - \varepsilon \frac{1}{2} \frac{\text{Re}(\mathbf{z})}{R_{\text{Ref}}}\right) - \varepsilon \frac{2}{n} \begin{pmatrix} \text{Im}\left[\left(\frac{\mathbf{z}}{R_{\text{Ref}}}\right)^n \mathbf{i}\right] \\ \text{Re}\left[\left(\frac{\mathbf{z}}{R_{\text{Ref}}}\right)^n\right] \end{pmatrix}, \quad (70)$$

or substituting $\mathbf{z}/R_{\text{Ref}}$ with $\rho e^{i\vartheta}$ one gets

$$\begin{pmatrix} \tilde{\tilde{\mathbf{T}}}_{\mathbf{m}}^{(\text{n})}(\mathbf{z}) \\ \tilde{\tilde{\mathbf{T}}}_{\mathbf{m}}^{(\text{s})}(\mathbf{z}) \end{pmatrix} = \rho^{n-1} e^{i(n-1)\vartheta} \left(1 - \varepsilon \rho \cos(\vartheta)\right) - \varepsilon \frac{\rho^n}{2n} \begin{pmatrix} \sin(n\vartheta) \mathbf{i} \\ \cos(n\vartheta) \end{pmatrix} \quad (71)$$

$$= \rho^{n-1} \left(e^{i(n-1)\vartheta} - \frac{\varepsilon \rho}{2} \left[e^{i(n-1)\vartheta} \cos(\vartheta) + \frac{1}{n} \begin{pmatrix} \sin(n\vartheta) \mathbf{i} \\ \cos(n\vartheta) \end{pmatrix} \right] \right) \quad (72)$$

in polar representation.

The second approach is using the expression Eq. (58) and derive the potential for the normal and skew multipoles as given in Eq. (9) and Eq. (11), as the first two term T_0 and T_1 are analytic and a complex representation of the solution facilitates interpretation. Given that $|\mathbf{z}|$ is part of the ansatz, the calculation can not be performed using complex coordinates safely. Instead these calculations were performed by two steps:

- At first all coordinates were substituted by their real values. Then the calculations were performed given by (60).

- Based on the results complex representations were deduced and Eqs. (63) and (64) were applied to verify the results. These equations are chosen such that the unperturbed term will produce the basis functions of conventional cylindrical circular multipoles.

These terms $\tilde{\tilde{\mathbf{T}}}_{\mathbf{m}}$ were calculated to high order using a computer algebra system [16]. Based on these results a formula was obtained and checked using [16] and MathematicaTM. Term 2 of Eq. (58) yields the following equation

$$\begin{pmatrix} \tilde{\tilde{\mathbf{T}}}_{\mathbf{m}}^{(\text{n})} \\ \tilde{\tilde{\mathbf{T}}}_{\mathbf{m}}^{(\text{s})} \end{pmatrix} = \left(\frac{\mathbf{z}}{R_{\text{Ref}}}\right)^2 (1-m) \left(\frac{\mathbf{z}}{R_{\text{Ref}}}\right)^{m-2} + \frac{2}{R_{\text{Ref}}^{m-1}} \begin{pmatrix} y \text{Re}(\mathbf{z}^{m-1} \mathbf{i}) - ix \text{Im}(\mathbf{z}^{m-1}) \\ -y \text{Im}(\mathbf{z}^{m-1} \mathbf{i}) - ix \text{Re}(\mathbf{z}^{m-1}) \end{pmatrix}, \quad (73)$$

which can be reformulated to

$$\begin{pmatrix} \tilde{\tilde{\mathbf{T}}}_{\mathbf{m}}^{(\text{n})} \\ \tilde{\tilde{\mathbf{T}}}_{\mathbf{m}}^{(\text{s})} \end{pmatrix} = \left(\frac{|\mathbf{z}|}{R_{\text{Ref}}}\right)^2 \frac{(m-1)}{m} \left(\frac{\mathbf{z}}{R_{\text{Ref}}}\right)^{m-2} + \frac{2\bar{\mathbf{z}}}{mR_{\text{Ref}}} \begin{pmatrix} \mathbf{i} \text{Im}\left(\left(\frac{\mathbf{z}}{R_{\text{Ref}}}\right)^{m-1}\right) \\ \text{Re}\left(\left(\frac{\mathbf{z}}{R_{\text{Ref}}}\right)^{m-1}\right) \end{pmatrix}, \quad (74)$$

with $\bar{\mathbf{z}} = x + iy$. The first basis functions for T_2 are given in Table III. For term T_0 and term T_1 one obtains

$$T_0 : \tilde{\tilde{\mathbf{T}}}_{\mathbf{m}}^{(\text{n})} = \tilde{\tilde{\mathbf{T}}}_{\mathbf{m}}^{(\text{s})} = \left(\frac{\mathbf{z}}{R_{\text{Ref}}}\right)^{m-1} \quad T_1 : \tilde{\tilde{\mathbf{T}}}_{\mathbf{m}}^{(\text{n})} = \tilde{\tilde{\mathbf{T}}}_{\mathbf{m}}^{(\text{s})} = \frac{m+1}{m} \left(\frac{\mathbf{z}}{R_{\text{Ref}}}\right)^m. \quad (75)$$

Thus term T_1 is a ‘‘feed-up’’, similar as a translation of coordinate systems gives a feed down. The results for these terms can be combined to

$$\begin{pmatrix} \tilde{\tilde{\mathbf{T}}}_{\mathbf{m}}^{(\text{n})} \\ \tilde{\tilde{\mathbf{T}}}_{\mathbf{m}}^{(\text{s})} \end{pmatrix} = \left(\frac{\mathbf{z}}{R_{\text{Ref}}}\right)^{m-1} - \frac{\varepsilon}{4m} \left\{ \left(\frac{\mathbf{z}}{R_{\text{Ref}}}\right)^{m-2} \left[(m+1) \left(\frac{\mathbf{z}}{R_{\text{Ref}}}\right)^2 + (m-1) \left| \left(\frac{\mathbf{z}}{R_{\text{Ref}}}\right) \right|^2 \right] + \frac{2\bar{\mathbf{z}}}{R_{\text{Ref}}} \begin{pmatrix} \mathbf{i} \text{Im}\left(\left(\frac{\mathbf{z}}{R_{\text{Ref}}}\right)^{m-1}\right) \\ \text{Re}\left(\left(\frac{\mathbf{z}}{R_{\text{Ref}}}\right)^{m-1}\right) \end{pmatrix} \right\}. \quad (76)$$

The results of the equation above were compared to Eq. (70) and found to be identical. The equation can be rewritten replacing $(\mathbf{z}/R_{\text{Ref}})$ with $\rho e^{i\vartheta}$.

$$\begin{pmatrix} \tilde{\tilde{\mathbf{T}}}_{\mathbf{m}}^{(\text{n})} \\ \tilde{\tilde{\mathbf{T}}}_{\mathbf{m}}^{(\text{s})} \end{pmatrix} = \rho^{m-1} e^{i(m-1)\vartheta} - \frac{\varepsilon}{4m} \left(\rho^{m+1} e^{i(m-2)\vartheta} \left[(m+1) e^{2i\vartheta} + (m-1) \right] + 2\rho^m e^{-i\vartheta} \begin{pmatrix} e^{i\pi/2} \sin((m-1)\vartheta) \\ \cos((m-1)\vartheta) \end{pmatrix} \right), \quad (77)$$

TABLE III. Potential and basis functions for term T_2 .

m	Φ	B_x	B_y
normal			
1	0	0	0
2	$-\frac{x^2 y}{R_{Ref}^3} - \frac{y^3}{R_{Ref}^3}$	$\frac{xy}{R_{Ref}^2}$	$\frac{x^2+3y^2}{2R_{Ref}^2}$
3	$-2\frac{x^3 y}{R_{Ref}^4} - 2\frac{xy^3}{R_{Ref}^4}$	$\frac{2}{3} \frac{y(3x^2+y^2)}{R_{Ref}^3}$	$\frac{2}{3} \frac{x(x^2+3y^2)}{R_{Ref}^3}$
4	$-3\frac{x^4 y}{R_{Ref}^5} - 2\frac{x^2 y^3}{R_{Ref}^5} + \frac{y^5}{R_{Ref}^5}$	$\frac{xy(3x^2+y^2)}{R_{Ref}^4}$	$\frac{3x^4+6x^2 y^2-5y^4}{4R_{Ref}^4}$
5	$-4\frac{x^5 y}{R_{Ref}^6} + 4\frac{xy^5}{R_{Ref}^6}$	$\frac{4}{5} \frac{y(5x^4-y^4)}{R_{Ref}^5}$	$\frac{4}{5} \frac{x(x^4-5y^4)}{R_{Ref}^5}$
skew			
1	$-\frac{x^2}{R_{Ref}^2} - \frac{y^2}{R_{Ref}^2}$	$2\frac{x}{R_{Ref}}$	$2\frac{y}{R_{Ref}}$
2	$-\frac{x^3}{R_{Ref}^3} - \frac{xy^2}{R_{Ref}^3}$	$\frac{3x^2+y^2}{2R_{Ref}^2}$	$\frac{xy}{R_{Ref}^2}$
3	$-\frac{x^4}{R_{Ref}^4} + \frac{y^4}{R_{Ref}^4}$	$\frac{4}{3} \frac{x^3}{R_{Ref}^3}$	$-\frac{4}{3} \frac{y^3}{R_{Ref}^3}$
4	$-\frac{x^5}{R_{Ref}^5} + 2\frac{x^3 y^2}{R_{Ref}^5} + 3\frac{xy^4}{R_{Ref}^5}$	$\frac{5x^4-6x^2 y^2-3y^4}{4R_{Ref}^4}$	$\frac{xy(-x^2-3y^2)}{R_{Ref}^4}$
5	$-\frac{x^6}{R_{Ref}^6} + 5\frac{x^4 y^2}{R_{Ref}^6} + 5\frac{x^2 y^4}{R_{Ref}^6} - \frac{y^6}{R_{Ref}^6}$	$\frac{6x^5-20x^3 y^2-10xy^4}{5R_{Ref}^5}$	$\frac{2}{5} \frac{y(-5x^4-10x^2 y^2+3y^4)}{R_{Ref}^5}$

It can be further transformed to

$$\begin{pmatrix} \tilde{\mathbf{T}}_{\mathbf{m}}^{(\mathbf{n})} \\ \tilde{\mathbf{T}}_{\mathbf{m}}^{(\mathbf{s})} \end{pmatrix} = \rho^{m-1} \left(e^{i(m-1)\vartheta} - \frac{\rho\epsilon}{4m} \left\{ e^{i(m-2)\vartheta} [(m+1)e^{2i\vartheta} + (m-1)] + 2e^{-i\vartheta} \begin{bmatrix} e^{i\pi/2} \sin((m-1)\vartheta) \\ \cos((m-1)\vartheta) \end{bmatrix} \right\} \right), \quad (78)$$

and

$$\begin{pmatrix} \tilde{\mathbf{T}}_{\mathbf{m}}^{(\mathbf{n})} \\ \tilde{\mathbf{T}}_{\mathbf{m}}^{(\mathbf{s})} \end{pmatrix} = \rho^{m-1} e^{i(m-1)\vartheta} \left(1 - \frac{\rho\epsilon}{4m} \left\{ [(m+1)e^{i\vartheta} + (m-1)e^{-i\vartheta}] + 2e^{-i\vartheta} \begin{bmatrix} e^{i\pi/2} \sin((m-1)\vartheta) \\ \cos((m-1)\vartheta) \end{bmatrix} \right\} \right). \quad (79)$$

The equations above are just reformulations of Eqs. (70) and (76) but simplify the understanding of the obtained results. One can see that

- the whole perturbation depends linearly on the offset from the centre circle.
- The distortions decrease for higher orders of m .
- The first term corresponds to a feed up, as if a multipole with order $\epsilon(m+1)/4$ was added. The other one corresponds to a field increasing with the distance from the centre circle.
- The last term, which is different for $\tilde{\mathbf{T}}^{\mathbf{n}}$ and $\tilde{\mathbf{T}}^{\mathbf{s}}$, is counter-rotating with the phase of the field. Finally $\tilde{\mathbf{T}}^{\mathbf{s}}$ is scaled by the imaginary component while $\tilde{\mathbf{T}}^{\mathbf{n}}$ is scaled by the real component of $\mathbf{z}/|\mathbf{z}|$ in the direction x .

The distortions are non harmonic solutions except for the feed up. The last term shows that the field is decreasing with increasing x . Given that the solution was obtained bending the basis functions and thus “the magnet”, these are not surprising. A straight air coil dipole magnet which is bent would show similar behaviour, as the current density decreases per length on the outside

but increases at the inside. The rotations follow similar insight, as the field direction should change too (imagine a straight sextupole coil which is bent to a torus).

D. Elliptic toroidal multipoles

1. Elliptic local toroidal coordinates

If instead of a circle an ellipse is revolved around the major circle (like pressing down a doughnut), an adapted coordinate system is a system of Local Elliptic Toroidal Coordinates. Thus the minor circle is replaced by an ellipse.

Its transform to Cartesian coordinates is given by ([2, 7] see also Fig. 2)

$$\begin{aligned} X &= (R_C + \bar{e} \cosh \bar{\eta} \cos \bar{\psi}) \cos \phi, \\ Y &= (R_C + \bar{e} \cosh \bar{\eta} \cos \bar{\psi}) \sin \phi, \\ Z &= \bar{e} \sinh \bar{\eta} \sin \bar{\psi}, \end{aligned} \quad (80)$$

with \bar{e} the eccentricity of the ellipse, $\bar{\eta}$ and $\bar{\psi}$ the coordinates of the ellipse equivalent to η and ψ in Eq. (13). The eccentricity of the ellipse is equivalent to the one for

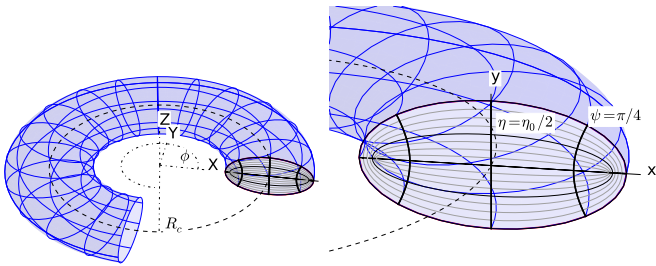


FIG. 2. The local elliptic toroidal coordinates. The left image gives the total torus while the right one shows the local coordinate system.

the elliptic cylinder coordinates [Eq. (13)]

$$\bar{e} = \sqrt{a^2 - b^2} \quad (81)$$

with a the major and b the minor axes of the ellipse. The major radius of the torus is R_C . The boundary of the volume is now an ellipse instead of a circle. Its surface is defined by $\bar{\eta}_0$

$$\tanh \bar{\eta}_0 = \frac{b}{a}. \quad (82)$$

The volume of interest is a segment of a torus given by

$$0 \leq \bar{\eta} \leq \bar{\eta}_0, \quad -\pi \leq \bar{\psi} \leq \pi, \quad -\phi_0 \leq \phi \leq \phi_0. \quad (83)$$

Equivalent to the ratio of minor to major radius ε one now defines

$$\bar{\varepsilon} := \frac{\bar{e}}{R_C}, \quad (84)$$

thus the ratio of the eccentricity over the major radius. The metric coefficients are then defined by

$$h_t = h_{\bar{\eta}} = \bar{h}_{\bar{\psi}} = \bar{e} \sqrt{\cosh(2\bar{\eta}) - \cos(2\bar{\psi})} / \sqrt{2}, \quad (85)$$

$$h_\phi = R_C + \bar{e} \cosh \bar{\eta} \cos \bar{\psi} \quad (86)$$

$$= R_C (1 + \bar{\varepsilon} \cosh \bar{\eta} \cos \bar{\psi}) = R_C \bar{h}. \quad (87)$$

Up to some unessential constant factor the Laplace operator for toroidally (azimuthally) uniform potentials is

$$\frac{1}{\cosh(2\bar{\eta}) - \cos(2\bar{\psi})} \times \left[\frac{\partial^2}{\partial \bar{\eta}^2} + \frac{\partial^2}{\partial \bar{\psi}^2} - \frac{\bar{\varepsilon}}{\bar{h}} \left(\sinh \bar{\eta} \cos \bar{\psi} \frac{\partial}{\partial \bar{\eta}} + \cosh \bar{\eta} \sin \bar{\psi} \frac{\partial}{\partial \bar{\eta}} \right) \right] \bar{\Psi} = 0. \quad (88)$$

The same approach is used as above for the local toroidal multipoles (see section II C 1): “bending the basis functions” is accomplished by replacing Φ with $\sqrt{\bar{h}} \bar{\Phi}$. This yields

$$\frac{1}{\sqrt{\bar{h}}} \times \left[\frac{\partial^2}{\partial \bar{\eta}^2} + \frac{\partial^2}{\partial \bar{\psi}^2} - \frac{\bar{\varepsilon}^2}{8\bar{h}^2} (\cosh(2\bar{\eta}) - \cos(2\bar{\psi})) \right] \left(\sqrt{\bar{h}} \bar{\Psi} \right) = 0. \quad (89)$$

As above any terms of order $\mathcal{O}(\bar{\varepsilon}^2)$ are neglected. The remaining part of the differential equation then resembles that for the elliptic cylindrical multipoles (see section II B). Suitable solutions of the latter equation must be identified with $\sqrt{\bar{h}} \bar{\Psi}$. Trials to do that in the same way as in the elliptic cylindrical case by using the cylindrical solutions for normal or skew elliptic cylindrical multipoles gave no satisfactory result. It is a task for the future to find suitable solutions.

III. MEASURING ADVANCED MULTIPOLES

The advanced multipole descriptions above are an extension to the standard description. Even if per se useful and furthering our understanding of magnetic fields in accelerators, these remain theoretical studies. In this chapter we show how these multipoles can be measured with rotating coil probes. The approach, the necessary measurement considerations and drawn conclusion are not limited to rotating coil probes but applicable to any device covering the curve of development similarly.

A. Excurs: Rotating coil probes

Rotating coil probes have been frequently used for measuring magnetic fields on a straight cylinder. In this paper only “radial” coil probes (see e.g. [17, 18]) will be considered (see also Fig. 8). One can show that their sensitivity \mathbf{K}_n of a so called radial coil probe is then defined by

$$\mathbf{K}_n = \frac{NLR_{Ref}}{n} \left[\left(\frac{r_2}{R_{Ref}} \right)^n - \left(\frac{r_1}{R_{Ref}} \right)^n \right] \quad (90)$$

with L the length of the coil probe, N its number of turns and r_2 the outer and r_1 the inner radius. Recording the induced signal, calculating its spectrum and scaling the spectrum with the sensitivity factors given above the harmonic content of the measured signal is obtained (e.g. [17]).

B. Measuring elliptic cylindrical multipoles

While one could consider measuring the field along the elliptic boundary and deducing harmonics from these measurements such measurements are impractical within an anticryostat, which is only of limited use as mechanical reference. Further these movements have to be made with an accuracy of several μm and are thus not simply applicable. Therefore a different approach is chosen here: the field is measured at different lateral positions using a rotating coil probe and the fields are then combined. A full description is given in [3], here only a short summary is given; it focuses on explaining the idea behind the method. This approach is not a mathematical rigorous

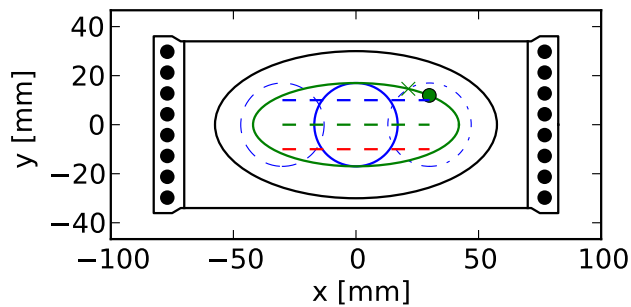


FIG. 3. Location of the coil probes (blue circles, solid line for the centre, dashed lines for the left and dashed dotted for the right measurement) within the magnet aperture together with the ellipse (in green) used for calculating the elliptic multipoles. The larger black ellipse gives the intended good field region. The straight dashed lines show the area covered by the mapper and its hall probe. The other lines depict the magnet aperture together with the 8 turn coil (each turn shown as black circle). The intersection between the ellipse and the circle are given by 'x' (with elliptic angle ψ_c). The green circle indicates $0.75 \cdot \psi_c$.

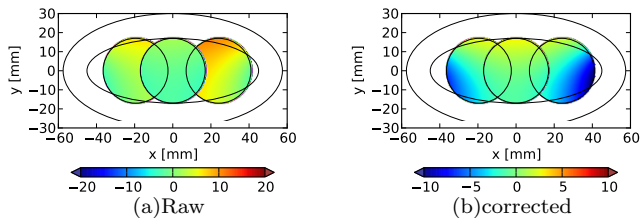


FIG. 4. Raw and corrected data as measured by the rotating coil probe for the field homogeneity ΔB_y for a nominal field of 1.9 T. Colour scale in units. 1 unit is equal to 100 ppm.

optimisation; it uses the features of rotating coil probes, in particular the ones of a compensation array. To the readers not familiar to rotating coil probes: the measurement presented in the following is applicable to any system, which gives more accurate results for the higher order harmonics than for the main one. This property implies that within the measurement area the field homogeneity is obtained more precisely than the absolute value. This property is used in the following.

The field is measured at different positions (see Fig. 3, [19, 20]) with a rotating coil probe. If the field is then plotted within the circles using the obtained multipole coefficients (see Fig. 4(a)), one will find that the field is not continuous in the overlapping area, which is a clear violation of the potential equation or $\nabla \cdot B = 0$. Therefore the measurements have to be corrected. The source of this deviation is the limited accuracy of the main field measurement. Now one adjusts the main field (in magnitude and direction), so that the error in the overlapping error gets minimal. We have been using this approach for evaluating the measurements of the SIS100 dipole model

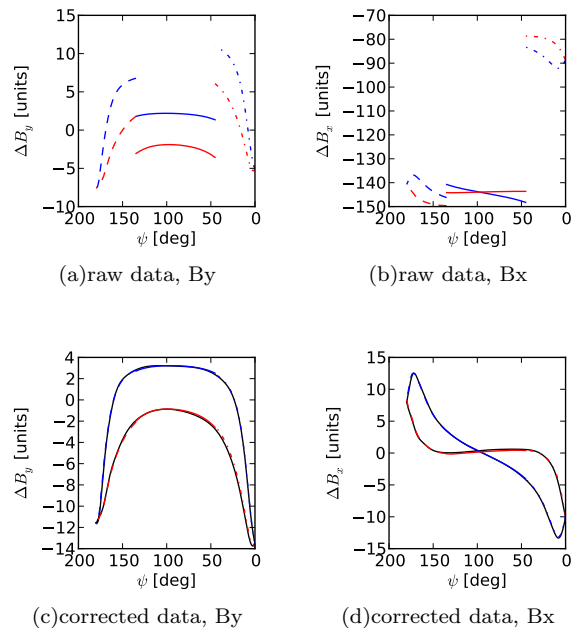


FIG. 5. Raw and corrected data as measured by the rotating coil probe for the field homogeneity ΔB_y for a nominal field of 1.9 T. All data is plotted along the ellipse versus the angle ψ . For angles from 0 to π the data are represented by blue lines for angles from $-\pi$ to 0 the data are represented by red lines. The solid lines represent the data where the multipoles of the central coil probe were used. The dashed lines where the multipoles of the measurement from the left side were used, and the dashed dotted lines where the multipoles of the measurement from the right side were used. For the left side the main multipole strength was corrected by ≈ 5 units and its angle by 15 mrad. For the right side the multipole strength was corrected by ≈ -8 units and its angle by ≈ 8 mrad. The black lines gives the field when the derived multipoles are used for reinterpolation.

magnets and the SIS100 first series magnet [20–22].

To apply this method one can plot the data along the ellipse for the field B_y and B_x along the ellipse (see Fig. 5(a) and Fig. 5(b)) for the different measurements along the path one will use later for reconstructing the field on the ellipse (the choice of length is given below). One can see that the field on the upper path and the lower path are shifted by more or less the same value and that, despite of the discontinuity, the curvature of the lines seems to be continuous. Now the absolute strength of only the main multipole and the angle of the main multipoles is corrected for the measurement at the left and the right until the lines are continuous. These parameters were adjusted manually using a computer program with graphical interface. The adaption of the strength of the main harmonic mainly affects B_y and the correction of the angle of the main harmonics mainly affects B_x . The data interpolated from each measurement and the data reconstructed from the elliptic multipoles are presented

in Fig. 5(c) and Fig. 5(d). The data represented by the solid blue and red line represent the measurement of the centre circle (as shown by the solid blue circle in Fig. 3). The x-scale of the sub-figures in Fig. 5 was plotted from right to left. It represents the angle ψ and hence the data obtained by the left measurement (shown as dash dotted line in Fig. 3) is also shown on the right in Fig. 5). One can see that the multipoles represent the original data significantly better than 0.1 units.

The last item that remains to clarify, is how one selects for which part of the ellipse one uses which measurement data and where the cutting angle is chosen. Only the first quadrant is discussed here, as the others are treated accordingly. The simplest approach were, to use the data within the measurement on the right as long as the ellipse is within the area of this measurement and to use the middle measurement for the rest in the quadrant. This approach is without physical justification. Further a discontinuity at the border of the measurement would be left over. So a more sophisticated method is required.

As start point the accuracy of the rotating coil probe measurement has to be estimated in space. The authors chose the distance of the point in question from the centre of rotation as weight function [3]. Then the data for the different points could be reconstructed for the different points B_i using

$$\mathbf{B}_i(\mathbf{z}) = \lambda B_1 e^{i\alpha} \sum_{n=2}^N \mathbf{c}_n \left(\frac{\mathbf{z}}{R_{Ref}} \right)^n + (1 - \lambda) B_1^r e^{i\alpha_r} \sum_{n=2}^N \mathbf{c}_n^{1,r} \left(\frac{\mathbf{z} - x_m}{R_{Ref}} \right)^n \quad (91)$$

for B^r and α_r along the ellipse η_0 . r indicate the right measurement and x_m the offset of the axis of rotation from the centre. N was chosen to 10 as all further measured multipoles were close to zero. The weight functions of the two measurements

$$w^r = \frac{R_m}{|\mathbf{z} - x_m|} \quad w^c = \frac{R_m}{|\mathbf{z}|} \quad (92)$$

is now combined to

$$\lambda^{cr} = \frac{w^c}{(w^c + w^r)}. \quad (93)$$

This λ^{cr} (see also Fig. 6 [3]) represents the weight functions of the two measurements for each position; but it is neither 0 nor 1 and the boundaries. Further it is desirable that the field and its derivative are continuous. A good approximation can be made for the first quadrant using the polynomial

$$\lambda(p_0) = 0, \quad \lambda(p_1) = 1, \quad \lambda'(p_0, p_1) = 0, \quad \lambda(p) = 3p^2 - 2p^3$$

with

$$p = \begin{cases} 0 & \psi < p_0 \\ \frac{2\psi - \pi}{2p_0 - \pi} & p_0 \leq \psi \leq \pi; \end{cases} \quad (94)$$

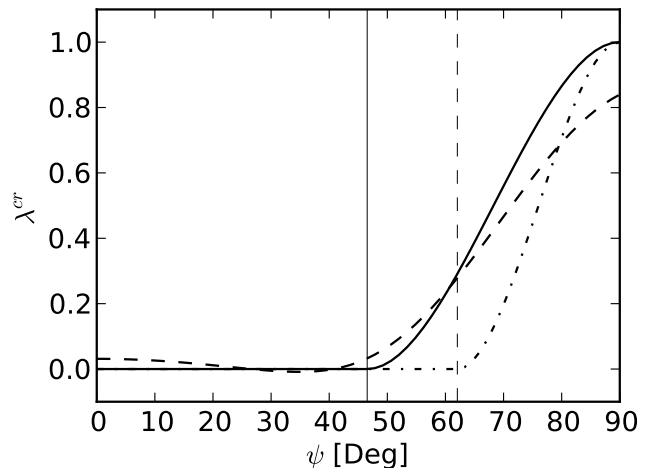


FIG. 6. The weights of the measurement as well as the interpolation functions versus the angle ψ for the first quadrant. The solid line indicates the function λ with $p_0 = 0.75\psi_c$ and the dashed dotted line the function λ with $p_0 = \psi_c$. The dashed line indicates the weight function for the measurement in the centre $2\lambda^{cr} - 0.5$. The scale and offset are used to facilitate the visual comparison to the function λ . The vertical dashed line indicates the angle ψ_c and the vertical solid line the angle $p_0 = 0.75\psi_c$.

see [3]. p_0 was chosen such that λ resembles the weight function as closely as possible: i.e $p_0 = 0.75\psi_c$, with ψ_c the cut angle at which the ellipse intersects the right measurement area. This definition of λ ensures that the interpolation is continuous in its function and its derivative.

The elliptic multipoles \mathbf{E}_n are then obtained by Fourier transform according to

$$\mathbf{E}_n = \frac{1}{\pi \mathcal{B}_0} \int_{-\pi}^{\pi} \mathbf{B}_0(\mathbf{z} = e \cosh(\eta_0 + i\psi)) \cos(n\psi) d\psi. \quad (95)$$

The data obtained by these measurements were cross checked using a hall probe along a mapper and scanning the field along the lines presented in Fig. 3. The comparison of these two measurements is presented for the end field of the SIS100 FoS dipole in Fig. 7. One can see that the two measurements match well. This proves that the method described here is sound and reliable and can be used for measuring accelerator magnets.

C. Measuring toroidal multipoles

The aperture of bending magnets (i.e. a dipole) in an accelerator can be reduced if the magnet is curved and thus it follows the sagitta of the beam. These magnets are typically measured with search coils, i.e. coil probes which follow the magnets curvature. These were used to measure SIS18 magnets [23] the magnets of HIT [24] or CNAO [25]. Skew multipoles can not be derived

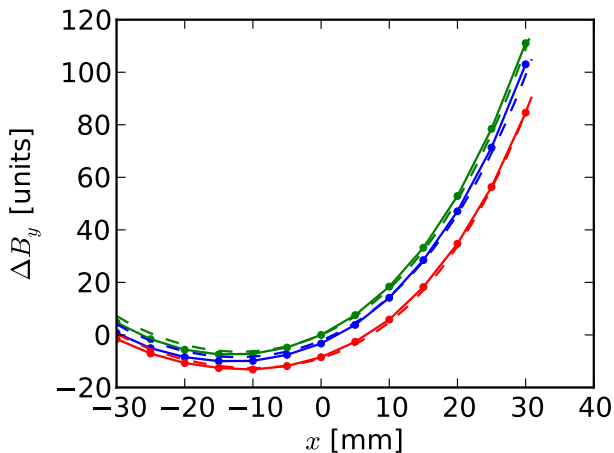


FIG. 7. Comparison of the mapper data to the coil probe data. The dots indicate the mapper data, the dashed lines the reconstructed field for the magnet end. In blue the data are given for a measurement position $y = +10$ mm, in green for $y = 0$ and in red for $y = -10$ mm.

from these measurements. Further the coil probe must be aligned with the mid-plane. For magnets, whose yoke is operated at cryogenic temperature, search coils operating at cryogenic temperature were not seen as an option. An anticryostat with a reference surface was studied but not found to be a good technical option as it reduces the aperture too much when the SIS100 dipole magnets have to be measured.

Therefore investigations were made if rotating coil probes can be used, as these can be operated within an anticryostat and allow measuring the integral harmonics content of the magnetic field. So their theoretical measuring capabilities were studied for curved accelerator magnets using the local toroidal multipoles.

1. Coordinate systems

The toroidal circular multipoles (see section II C 1) allow deriving the limits of a rotating coil measurement. The results given here are based on [6, 7]. The integrations are made similarly as for a straight magnet, but now the dependence of the field along the direction of the rotation axis must be taken into account [6]. Here one assumes that the field is constant versus the toroidal angle ϕ , with the multipoles as given in Eq. (61) (see Fig. 8). In the following only one half of the coil probe is considered (i.e. longitudinally from the middle, where the coil axis touches the torus centre circle up to one end to avoid that some symmetric contributions would cancel).

Several coordinate systems are needed to deal with this complex situation. The local Cartesian coordinates x, y have been introduced in section II C 1. We assume that

the axis of the rotating wire frame is parallel to the equatorial plane. The centre of the frame has the coordinates $x = d_x, y = d_y, \phi = 0$. We introduce cylindrical coordinates r, ϑ, z , whose z -axis coincides with the rotation axis; the origin is at the centre of the wire frame. The relation of the various local coordinates to the global Cartesian ones is given by

$$X = (R_C + x) \cos \phi = R_C + d_x + r \cos \vartheta, \quad (96)$$

$$Y = (R_C + x) \sin \phi = -z, \quad (97)$$

$$Z = y = d_y + r \sin \vartheta. \quad (98)$$

Analytic relations between these various variables of these sets are needed for computing the magnetic flux penetrating the coil probe. Some of these relations cannot be given exactly; again approximations up to the first order in ε are introduced. This is done for a fixed inclination angle ϑ of the coil's frame.

For that purpose one uses the local Cartesian system of the toroidal multipoles (see section II C 1 a and Fig. 9). From Eqs. (96) and (97) follows

$$\tan \varphi = \frac{Y}{X} = \frac{-z}{R_C + d_x + r \cos \vartheta} \quad (99)$$

the dependence of φ on the cylindrical variables. From this in turn we get:

$$\cos \varphi = \frac{1}{\sqrt{1 + \tan^2 \varphi}} = \frac{R_C + d_x + r \cos \vartheta}{\sqrt{R_C + d_x + r \cos \vartheta + z^2}}, \quad (100)$$

Now we substitute $R_C = R_{Ref}/\varepsilon$ and calculate the series which yields

$$\cos \varphi = \frac{-z}{R_C + d_x + r \cos \vartheta} = 1 - \varepsilon^2 \frac{z^2}{2R_{Ref}^2} = 1 + \mathcal{O}(\varepsilon^2). \quad (101)$$

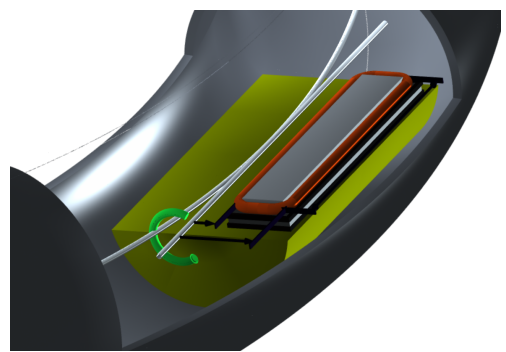


FIG. 8. The rotating coil within a torus. The torus has been cut open so that the coil is visible. The centre line of the torus is indicated together with the rotation axis of the coil. The coil is indicated as a single turn. The rotation axis is a tangent to the torus. The centre of the rotating coil is also the point where the tangent touches the centre circle.

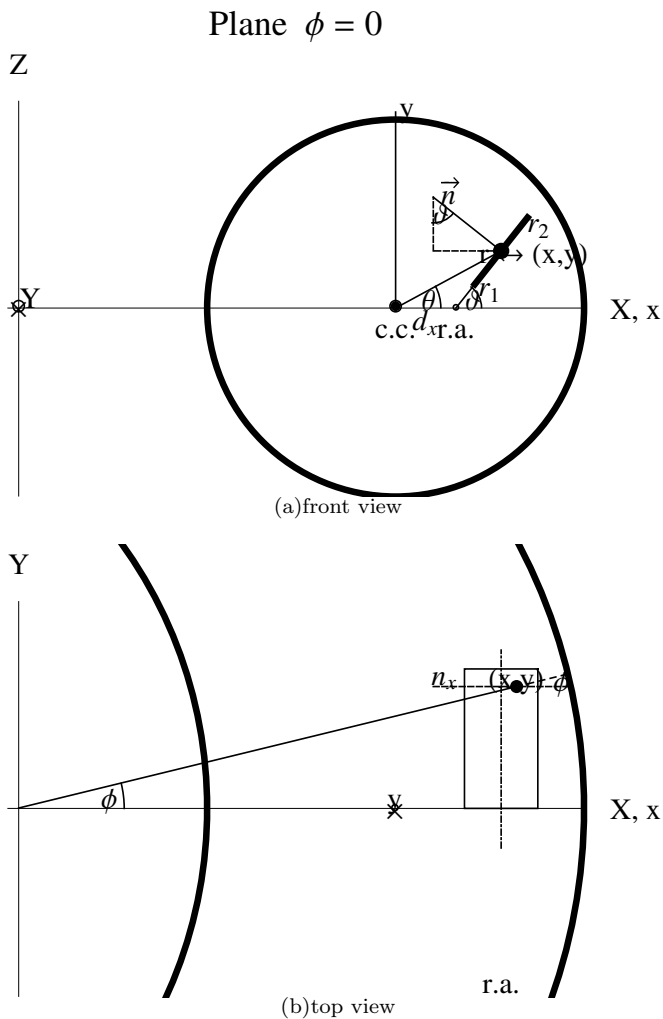


FIG. 9. Illustration of the coil and integration paths. The top figure shows the view from the front and the bottom the view from the top. r_1 and r_2 are the inner and outer radius of the coil probe, d the offset of the coil probe rotation axis from the ideal axis, z the longitudinal offset in the local coordinate frame x, y, z .

Inserting Eq. (101) in Eq. (96) yields

$$\begin{aligned}
 x &= \frac{R_C + d_x + r \cos \vartheta}{\cos \varphi} - R_C & (102) \\
 &= \sqrt{(R_C + d_x + r \cos \vartheta)^2 - R_C^2} \\
 &= R_C \left[1 + \frac{d_x + r \cos \vartheta}{R_C} + \frac{z^2}{2R_C^2} + \dots - 1 \right]. & (103)
 \end{aligned}$$

With these formulas the change in the x position versus z due to the sagitta is given by

$$x = \chi_x(r, \vartheta, z) := d_x + r \cos \vartheta + \varepsilon \frac{z^2}{2R_{Ref}} + \mathcal{O}(\varepsilon^2), \quad (104)$$

which approximates the larger torus circle with an

parabola. According to Eq. (98), y is given by

$$y = \chi_y(r, \vartheta, z) := d_y + r \sin \vartheta. \quad (105)$$

2. The magnetic flux

The flux penetrating a coil probe (e.g. [17]) is given by

$$\Phi = \int_{r_1}^{r_2} \int_0^L \mathbf{B}_n \, dz \, dr. \quad (106)$$

\mathbf{B}_n is the magnetic induction normal to the wire frame.

When calculating this quantity we must take into account that both the values of the local Cartesian variable change with r, ϑ, z as given in Eqs. (104) and (105) and that the field components are transformed. In a Cartesian system corresponding to the cylindrical system defined above, the normal is the unity vector \vec{n}' :

$$\begin{aligned}
 \vec{n}' &= (-\sin \vartheta', \cos \vartheta', 0), \\
 \vec{n} &= (-\sin \vartheta \cos \phi, \cos \vartheta, \sin \vartheta \sin \phi). & (107)
 \end{aligned}$$

The angle ϑ gives the instantaneous inclination of the wire frame w.r.t. the equatorial plane defined by the X- and Y-axes (see Fig. 9(a)). The normal \vec{n} is erected in the plane $\phi = \text{const}$ in the local Cartesian system x, y, z . It is assumed that the B_x and B_y are invariant versus ϕ . B_y is the same in this plane and in any other plane $z = \text{const}$. In the transformation from the planes defined in the local Cartesian system to the local toroidal one the components B_x and the third component are involved. The latter is zero; the first one contributes to B'_x and B'_z so we get (see Fig. 9(b))

$$\vec{B}' = (B'_x, B'_y, B'_z) = (B_x \cos \phi, B_y, B_x \sin \phi). \quad (108)$$

The coil probe is not sensitive to B'_z . The final expression for the component of the magnetic induction normal to the coil probe is:

$$\begin{aligned}
 \mathbf{B}_n &= (\vec{n}' \cdot \vec{B}') = (\vec{n} \cdot \vec{B}) = \\
 &= -B_x (\chi_x(r, \vartheta, z), \chi_y(r, \vartheta, z)) \sin \vartheta \cos \phi + \\
 &\quad + B_y (\chi_x(r, \vartheta, z), \chi_y(r, \vartheta, z)) \cos \vartheta. & (109)
 \end{aligned}$$

For the magnetic induction the expansion Eq. (61) is inserted into Eq. (109) with x [Eqs. (104)] and y [Eq. (105)] replaced as just shown thus

$$\mathbf{B}_n = \sum_{m=1}^M [\bar{B}_m (\mathbf{T}_m^{Cn}(\chi_x, \chi_y) \cdot \vec{n}) + \bar{A}_m (\mathbf{T}_m^{Cs}(\chi_x, \chi_y) \cdot \vec{n})]. \quad (110)$$

The z -component of the surface normal to the coil area [Eq. (107)] can be set to zero as the coil probe is insensitive to B_z . The integration is over r and z but takes the

curvature of the torus into account in the usual approximation (first order in ε); so the flux seen by the coil with inclination ϑ is given by

$$\Phi(\vartheta) = \int_0^L \int_{r_1}^{r_2} \mathbf{B}_n \, dr \, dz. \quad (111)$$

The integrals in this equation may be expressed in the following way after lengthy calculations performed with a computer algebra system (MathematicaTM):

$$\begin{aligned} \int_0^L \int_{r_1}^{r_2} (\mathbf{T}_\mu^{Cn}(\chi_x, \chi_y) \cdot \vec{n}) \, dr \, dz &= \quad (112) \\ &= \frac{1}{N} \sum_{\nu=1}^{M+1} [G_{\mu\nu}^{nc} K_\nu \cos(\nu\vartheta) + G_{\mu\nu}^{ns} K_\nu \sin(\nu\vartheta)], \\ &\quad \mu = 1, 2, \dots, M, \quad (113) \end{aligned}$$

$$\begin{aligned} \int_0^L \int_{r_1}^{r_2} (\mathbf{T}_\mu^{Cs}(\chi_x, \chi_y) \cdot \vec{n}) \, dr \, dz &= \quad (114) \\ &= \frac{1}{N} \sum_{\nu=1}^{M+1} [G_{\mu\nu}^{ss} K_\nu \sin(\nu\vartheta) + G_{\mu\nu}^{sc} K_\nu \cos(\nu\vartheta)]. \end{aligned}$$

For the upper limit $M = 20$ is used; This gives sufficient accuracy for the applications we have in mind. simpler expressions could not be derived using the terms of Eq. (70) separately. Inspection of the elements of these four matrices show 1's, -1's respectively in the main diagonal of G^{nc} , G^{ss} respectively. All other elements are zero or their absolute values are appreciably smaller than unity. Therefore we define:

$$\begin{aligned} G_{\mu\nu}^{nc} &= \delta_{\mu\nu} + H_{\mu\nu}^{nc}, \\ G_{\mu\nu}^{ss} &= -\delta_{\mu\nu} + H_{\mu\nu}^{ss}, \\ &\quad \mu, \nu = 1, 2, \dots, M, \quad (115) \\ G_{\mu\nu}^{ns} &= H_{\mu\nu}^{ns}, \\ G_{\mu\nu}^{sc} &= H_{\mu\nu}^{sc}. \end{aligned}$$

The resulting $M \times M$ matrices are used to define a $2M \times 2M$ matrix:

$$G := G^o + H = G^o + \begin{pmatrix} H^{nc} & H^{ns} \\ H^{sc} & H^{ss} \end{pmatrix} \quad (116)$$

The $2M \times 2M$ matrix G^o is a diagonal matrix comprising M 1, then M -1's:

$$G^o = \text{dia}(1, 1, 1, \dots, \dots, -1, -1, 1) = (G^o)^{-1}. \quad (117)$$

The elements in columns 2 to M of the $M \times M$ matrices are the same (or the opposite) at corresponding places:

$$G^{nc} + G^{ss} = H^{nc} + H^{ss} = (H^r, 0, 0, 0, \dots), \quad (118)$$

$$G^{ns} - G^{sc} = H^{ns} - H^{sc} = (H^i, 0, 0, 0, \dots); \quad (119)$$

$$(H^r + \mathbf{i}H^i)_k = \varepsilon \mathbf{d}\mathbf{z}^k / (2kR_{Ref}^k), \mathbf{d}\mathbf{z} = dx + \mathbf{i}dy. \quad (120)$$

In the brackets at the end of the first two lines of the above equations the first columns are listed. Only the first column contains elements different from zero; which

are given in the last line, the label k denotes the k -th row of this first column.

The flux $\Phi(\vartheta)$ may then be written as:

$$\Phi(\vartheta) = \frac{1}{N} (B, A) \cdot G \cdot K \cdot v \quad (121)$$

where K is a diagonal matrix containing the M sensitivities twice:

$$K := \text{dia}(K_1, K_2, \dots, K_M, K_1, K_2, \dots, K_M); \quad (122)$$

(B, A) denotes a row vector comprising the $M + M$ expansion coefficients:

$$(B, A) = (B_1, B_2, B_3, \dots, B_M, A_1, A_2, A_3, \dots, A_M); \quad (123)$$

The column vector v contains the M harmonics $\cos(\nu\vartheta)$ at first, then the M harmonics $\sin(\nu\vartheta)$:

$$\begin{aligned} v &= (\cos(\vartheta), \cos(2\vartheta), \dots, \cos(M\vartheta), \\ &\quad \sin(\vartheta), \sin(2\vartheta), \dots, \sin(M\vartheta)). \quad (124) \end{aligned}$$

Integrating Faraday's law with respect to time

$$\int V(t) dt = -N \int \int_{\mathcal{F}} \mathbf{B}_n \, dr \, dz. \quad (125)$$

integrating a Fourier expansion of the Voltage induced in the coil

$$\int V(t) dt = \sum_{n=1}^M [a_n \cos(n\omega t) + b_n \sin(n\omega t)] \quad (126)$$

and identifying $\vartheta = \omega t$ assuming that the coil rotates with constant angular velocity ω we finally get:

$$(a, b) \cdot v = - (B, A) \cdot G \cdot K \cdot v, \quad (127)$$

$$(B, A) = - (a, b) \cdot K^{-1} \cdot G^{-1}. \quad (128)$$

(a, b) denotes the row vector comprising the Fourier coefficients of the signal in the rotating radial coil:

$$(a, b) = (a_1, a_2, \dots, a_8, b_1, b_2, \dots, b_8). \quad (129)$$

A good approximation for the inverse of the matrix G is given by :

$$G^{-1} \approx G^o - G^o \cdot H \cdot G^o. \quad (130)$$

3. Conversion matrices

The sections given above showed that the toroidal multipoles can be deduced from rotating coil probe measurements assuming that these are uniform over the measurement length. The calculations above also considered the effect of a misplaced coil. The multipoles are mapped to the complex multipoles by

$$\begin{pmatrix} \mathbf{T}_\mu^{Cn} \\ \mathbf{T}_\mu^{Cs} \end{pmatrix} = \begin{pmatrix} G^{nc} & G^{ns} \\ G^{sc} & G^{ss} \end{pmatrix} \begin{pmatrix} \vec{B}_n \\ \vec{A}_n \end{pmatrix}. \quad (131)$$

Each of the submatrices G^{nc} , G^{ns} , G^{sc} and G^{ss} is set up by

$$G = I + \mathcal{L}^{dr} + \epsilon (\mathcal{L}^L + U + \mathcal{L}^{sk} + \mathcal{L}^{R2_0} + \mathcal{L}^{R2}). \quad (132)$$

Only elements of \mathcal{L}^L depend on the coil length L while only elements of \mathcal{L}^{sk} depend on the coil sensitivity parameters [Eq. (90)]. The elements of the last matrix depend only on d_x and d_y . All these matrices can be derived from complex matrices, but the result itself is not analytic. In the following part the coefficients of the different submatrices will be given.

The matrix U is the sole one which consists of constant terms and is given by

$$U = \frac{n+1}{4n} \delta_{n+1,m}. \quad (133)$$

Many of the matrices below are given as triangular lower matrices. Therefore one defines

$$\mathcal{L}_{n,m} = \begin{cases} 1 & n \geq m \\ 0 & n < m. \end{cases} \quad (134)$$

Similar to measuring with rotating coil probes, an offset of the coil probe causes that one multipole creates spurious other multipoles. These are similar for the different submatrices of matrix H and thus summarised here. The matrix \mathcal{L}^{dr} is the only one, which does not depend on the torus curvature ratio ϵ . Its non zero elements are given by

$$\mathcal{L}_{n,m}^{dr} = \binom{n-1}{m-1} \left(\frac{d_x + id_y}{R_{Ref}} \right)^{n-m} * \mathcal{L}_{n,m} - I. \quad (135)$$

The “*” denotes that these multiplication is to be made element wise. This term is due to the frame translation in d_x and d_y , which is exactly the same as found if a rotating coil probe is displaced by $d_x + id_y$ within a cylindrical circular coordinated system. This effect is called the “feed-down” effect. The identity matrix is subtracted as the diagonal has to be singled out for later treatment.

For describing \mathcal{L}^{dr2} one defines

$$\mathcal{L}_{n,m}^d = \begin{cases} 1 & n > m + 1 \\ 0 & n \leq m + 1. \end{cases} \quad (136)$$

Then \mathcal{L}^{dr2} is given by

$$\begin{aligned} \mathcal{L}_{n,m}^{dr2} &= (n-m) \binom{n-1}{m-1} \left(\frac{d_x + id_y}{R_{Ref}} \right)^{n-m-1} * \mathcal{L}_{n,m}^d + \\ &+ m \delta_{n,m+1} = R_{Ref} \frac{d}{dz} \mathcal{L}^{dr} \end{aligned} \quad (137)$$

and is similar to Eq. (135) except for the binomial factor and that the power is reduced by 1. The dependence on L is given by

$$\mathcal{L}_{n,m}^L = \frac{L^2}{3R_{Ref}^2} \mathcal{L}^{dr2}. \quad (138)$$

TABLE IV. Parameters for different machines.

	R_C [m]	R_{Ref} [mm]	ϵ [units]	L [mm]	d_x, d_y [mm]
LHC	2804	17	0.04	600	1
SIS100	52.5	40	7.62	600	1
SIS300	52.5	35	6.67	600	1
NICA	15	40	26.67	600	1

Please note, that the first side band includes the constant term $L^2/(3R_{Ref}^2)$. The dependence on the coil sensitivity factors \mathbf{K}_n is given by

$$\mathcal{L}_{n,m}^{sk} = \frac{1}{4(m+1)} * \frac{\mathbf{K}_{m+2}}{\mathbf{K}_m} * \mathcal{L}^{dr2}. \quad (139)$$

The most complex matrix does only depend on d_x and d_y . It is given by

$$\begin{aligned} \mathcal{L}_{n,m}^{R2} &= \left(\frac{nm}{n-m+1} * \mathcal{L}_{n,m} + \delta_{m,1} \right) * \\ &* \left[\frac{d_y}{R_{Ref}} - \left(\frac{2-m+2n}{m} * \mathcal{L}_{n,m} - n\delta_{m,1} \right) i \frac{d_x}{R_{Ref}} \right] * \\ &* \frac{1}{4n} * (\mathcal{L}^{dr} + I). \end{aligned} \quad (140)$$

The last matrix \mathcal{L}^{R2_0} is given by

$$\mathcal{L}_{n,m}^{R2_0} = \frac{1}{2n} \left(\frac{d_x + id_y}{R_{Ref}} \right)^n \delta_{m,1}. \quad (141)$$

Each of the submatrices G^{nc} , G^{ns} , G^{sc} and G^{ss} is set up by

$$\begin{aligned} G^{nc} &= I + \text{Re} [\mathcal{L}^{dr}] + \epsilon (-U + \text{Re} [\mathcal{L}^L] - \text{Re} [\mathcal{L}^{sk}] \\ &\quad + \text{Im} [\mathcal{L}^{R2}] + \text{Re} [\mathcal{L}^{R2_0}]), \\ G^{ns} &= -\text{Im} [\mathcal{L}^{dr}] + \epsilon (-\text{Im} [\mathcal{L}^L] + \text{Im} [\mathcal{L}^{sk}] \\ &\quad + \text{Re} [\mathcal{L}^{R2}]), \\ G^{sc} &= -\text{Im} [\mathcal{L}^{dr}] + \epsilon (-\text{Im} [\mathcal{L}^L] + \text{Im} [\mathcal{L}^{sk}] \\ &\quad + \text{Re} [\mathcal{L}^{R2}] - \text{Im} [\mathcal{L}^{R2_0}]), \\ G^{ss} &= -I - \text{Re} [\mathcal{L}^{dr}] + \epsilon (+U - \text{Re} [\mathcal{L}^L] + \text{Re} [\mathcal{L}^{sk}] \\ &\quad - \text{Im} [\mathcal{L}^{R2}]). \end{aligned} \quad (142)$$

This summary already shows that the main dipole is affected by all measured harmonics. On the other hand ϵ is rather small for the machines used here. The different matrices H are obtained omitting the identity matrices. Comparing the operators Re and Im on \mathcal{L}^L and \mathcal{L}^{sk} to the ones operating on \mathcal{L}^{dr} in Eq. (142) one can assume that \mathcal{L}^L and $-\mathcal{L}^{sk}$ are analytic.

4. Choosing a coil probe length

Evaluating all the different terms one can see that only \mathcal{L}^L is of significant size for accelerator magnets with characteristic values as given in Table IV. A criterion can be given for defining an adequate coil probe length by demanding that the feed down effect as found for cylindrical

circular multipoles and for measuring toroidal circular multipoles should be of equivalent size.

For describing the relation one defines $\mathcal{L}_{n,m}^{dL}$

$$\mathcal{L}_{n,m}^{dL} = \begin{cases} 1 & n > m \\ 0 & n \leq m + 1. \end{cases} \quad (143)$$

Then the relation can be given by

$$\mathcal{L}_{n,m}^{dr} = \underbrace{\frac{3R_{Ref}^2}{\epsilon L^2} \frac{d_x + id_y}{R_{Ref}}}_{L_s} \left(\frac{1}{n-m} \mathcal{L}_{n,m}^{dL} \right) * \mathcal{L}_{n,m}^L. \quad (144)$$

Demanding that the feed down effect due to coordinate translation \mathcal{L}^{dr} shall be similar to \mathcal{L}^L then $L_s = 1$ which yields as relation for the coil length

$$L = \sqrt{\frac{3(d_x + id_y)R_{Ref}}{\epsilon}} = \sqrt{3(d_x + id_y)R_C}, \quad (145)$$

using only the first side band ($n-m = 1$). Higher harmonics will be affected by larger spurious harmonics due to \mathcal{L}^L . As one can see the to be chosen coil length L becomes larger when the displacement errors d_x and d_y get smaller. On the other hand a smaller d_x or d_y will create smaller total spurious harmonics, and thus the overall contribution gets small. Decreasing d_x and d_y by a magnitude will only allow increasing the coil length by a factor of 3. It is recommended to evaluate the above equation for the maximum accepted deviations d_x, d_y . If a longer coil probe is chosen more effort shall be taken to determine d_x and d_y so that an appropriate treatment of the feed down effect can be made.

The attention of readers familiar to coil probes and evaluating their measurements shall be drawn to the influence of the sensitivity factors [Eq. (139)]. The first term affecting the ‘‘dipole’’ is the ‘‘sextupole’’ term. Here the ratio can be very small, if compensating systems or ‘‘bucking’’ systems are used (see e.g. [17]). Any further treatment will require to invert the matrices Eq. (142); in this case the sign of the term will swap and its magnitude change should be rather small, given that the identity matrix is involved.

5. Magnitude of the terms

The formulae given above were evaluated for the following different machines: the Large Hadron Collider (LHC) at CERN[26], SIS100 [27, 28] and SIS300 at GSI, and NICA [29, 30] at Dubna (see Table IV). The parameters given in Table IV were used to calculate the coefficients of the matrices. Accelerators require a field description with an accuracy of 1 unit and roughly 0.1 unit for the field homogeneity (1 unit equals 100 ppm). Therefore any contribution less than 1 ppm can be ignored.

Due to the circumference of the LHC ϵ is very small and thus the correction of all matrices are very small

(less than 1 ppm) except for the matrix \mathcal{L}^L , where the values close to the diagonal get to a size of 2000 ppm for $d = R_{Ref}$. So even for an insane value of d_z the artefacts are handable. This value may seem to exceed the target value for the field description; but the higher order multipoles are in the order of 100 ppm; thus the effective artifact will be safely below the target value of 10 ppm.

For machines with an aspect ratio as found for SIS100 or SIS300 the matrix U is in the order of 100 ppm. It can be neglected except for the main multipole. The values of the matrix \mathcal{L}^L get of similar size as the values for \mathcal{L}^{dr} . The magnitude of these values are defined by the magnitude of the offset $|d_x + id_y|$. Also when measuring straight magnets special methods are applied to obtain the offset d from the measured dataset [17]. Therefore one can assume that the artifacts can be minimised by similar adequate procedures.

The parameters for the different machines are given in Table IV. A practical coil length was deduced imposing that the influence of the offset of the coil from the straight line shall be of the same order as for a coil probe measuring a straight magnet [Eq. 145]. Now the matrices are evaluated to see to which extend different toroidal multipoles correspond to one measured multipole B_n or A_n .

The matrix Eq. (142) was evaluated. For the geometry of the machines considered here, as listed in Table IV, only the terms U and \mathcal{L}^L have a significant contribution; thus only the expression $U + \mathcal{L}^L$ is evaluated below. It is given by

$$C_1 = U + \mathcal{L}^L \quad (146)$$

$$= \begin{pmatrix} \cdot & \frac{1}{2} & & & & \\ \frac{L^2}{3R_{Ref}^2} & \cdot & \frac{3}{8} & & & \\ \frac{2L^2 d_z}{3R_{Ref}^3} & \frac{2L^2}{3R_{Ref}^2} & \cdot & \frac{1}{3} & & \\ \frac{L^2 d_z^2}{R_{Ref}^4} & \frac{2L^2 d_z}{R_{Ref}^3} & \frac{L^2}{R_{Ref}^2} & \cdot & \frac{5}{16} & \\ \frac{4L^2 d_z^3}{3R_{Ref}^5} & \frac{4L^2 d_z^2}{R_{Ref}^4} & \frac{4L^2 d_z}{R_{Ref}^3} & \frac{4L^2}{3R_{Ref}^2} & \cdot & \frac{3}{10} \\ \frac{5L^2 d_z^4}{3R_{Ref}^6} & \frac{20L^2 d_z^3}{3R_{Ref}^5} & \frac{10L^2 d_z^2}{R_{Ref}^4} & \frac{20L^2 d_z}{3R_{Ref}^3} & \frac{5L^2}{3R_{Ref}^2} & \cdot \end{pmatrix}.$$

The dots indicate the diagonal, where all elements are zero. The parameters given in Table IV were inserted. The matrix C was inverted which gives

$$C^{-1} = I + \frac{1}{10000} \begin{pmatrix} \cdot & 4 & \cdot & & & \\ 143 & \cdot & 3 & & & \\ 3 & 285 & \cdot & 3 & & \\ 9 & 428 & \cdot & 2 & & \\ -1 & 18 & 570 & \cdot & & \\ \cdot & -2 & 31 & 713 & \cdot & \\ \cdot & \cdot & -3 & 46 & \cdot & \\ \cdot & \cdot & \cdot & -6 & \cdot & \end{pmatrix}, \quad (147)$$

with all elements rounded to 1 unit. Elements smaller than one unit were left out. The dots indicate again the diagonal. The higher order harmonics, measured with the coil probe are in the order of some units. The basis

terms of the toroidal circular multipoles [Eq. (76)] are scaled with $\epsilon/4$ and the magnitude of term T_1 and T_2 is still less than 2. For accelerator magnets one can safely assume that all higher order harmonics are well below 10 units. So one can conclude that the effect of this matrix can be neglected for all measured harmonics except the main one if an field description accuracy of not better than $\frac{\epsilon}{4} \frac{10}{10000}$ is required. The toroidal circular term (see Table III and Eq. (76)) for $m = 1$ gives also a quadrupole and a term caused by Term T_2 ; thus the perturbation term is then exactly zero for the normal part. The skew part is $4x/R_{Ref}$ (see Table III), but this can be neglected as the skew component is small (< 10 units) and still has to be multiplied with ϵ . Therefore only a quadrupole of $\approx 140 \approx 20\epsilon$ units and a sextupole of ≈ 3 units has to be added to the set of cylindric circular multipoles. Then the cylindric circular multipole description can be used.

A measurement procedure for obtaining elliptic circular multipoles was given in section III B, with the measurements performed at different circles: in the centre of the magnet and shifted by $\delta x = \pm 30 \text{ mm}$. So one can define

$$R_C^\pm = R_C \pm \delta x \quad \text{and} \quad \epsilon^\pm = \frac{R_{Ref}}{R_C \pm \delta x}. \quad (148)$$

The different ϵ are then given by (in units)

$$\epsilon^\pm = 7.6009 \pm 0.0043 \quad (149)$$

using the values for SIS100 given in Table IV. The change of ϵ is at the 7th digit and is thus significantly smaller than the measurement accuracy obtainable with the systems given here. This result shows that the cylindric elliptic multipoles can be used to treat the measurements of the curved dipole magnets of SIS100.

The calculations for SIS300 yield a matrix with numerical values of

$$C_{SIS300}^{-1} = I - \frac{1}{10000} \begin{pmatrix} . & 3 & . & . & . \\ 125 & . & 2 & . & . \\ 3 & 249 & . & 2 & . \\ 9 & 374 & . & 2 & . \\ . & 19 & 499 & . & . \\ . & . & -1 & 31 & 624 \\ . & . & . & -2 & 47 \\ . & . & . & . & -4 \end{pmatrix} \quad (150)$$

thus the effect of curvature can be neglected for a coil

probe length of 600 mm, if the quadrupole is recalculated. The SIS300 magnets have a round aperture; thus different coil positions do not need to be evaluated.

The inverse of matrix C_{NICA} [29, 30] is given by

$$C_{NICA}^{-1} = I + \frac{1}{10000} \begin{pmatrix} -1 & 13 & . & . & . & . \\ 500 & -2 & 10 & . & . & . \\ -25 & 1000 & -2 & 9 & . & . \\ 1 & -75 & 1500 & -3 & 8 & . \\ . & 4 & -150 & 2001 & -4 & . \\ . & . & 9 & -250 & 2501 & . \\ . & . & . & 19 & -375 & . \\ . & . & . & 1 & 33 & . \end{pmatrix}, \quad (151)$$

which shows that the effects roughly increase with l/R'_C . Using the same δx , but $R'_C = 15 \text{ m}$ one gets

$$\epsilon_{NICA}^\pm \approx 26.67 \pm 0.053, \quad (152)$$

with ϵ_{NICA} in units. The values of the matrix C_{NICA}^{-1} are roughly three times higher than for C^{-1} (SIS100). Similarly ϵ_{NICA} is an order bigger than ϵ for SIS100. These influence will have to be evaluated and compared to the required field quality descriptions to see if the evaluation using circular multipoles is still precise enough.

IV. CONCLUSIONS

In this paper we presented 4 different set of multipoles: cylindric circular multipoles, cylindric elliptic multipoles, toroidal circular multipoles and toroidal elliptic multipoles. While the first is common practice, the others are to be considered advanced. The cylindric circular and elliptic multipoles are exact solutions of the potential equation while the later ones are approximative ones. The elliptic ones give a concise description within the beam vacuum chamber while the toroidal ones are approximation of the first order. These approximative ones are more straightforward to handle and to interpret than their alternative the global toroidal coordinates.

Measurement methods, based on rotating coil probes, have been theoretically investigated. The validity of the cylindric elliptic ones has been demonstrated on the SIS100 FoS dipole magnet comparing the field representation to mapper data.

-
- [1] P. Schnizer, B. Schnizer, P. Akishin, and E. Fischer, *Field Representation for Elliptic Apertures*, Tech. Rep. (Gesellschaft für Schwerionenforschung mbH, Planckstraße 1, D-64291 Darmstadt, 2007).
 [2] P. Schnizer, B. Schnizer, P. Akishin, A. Mierau, and E. Fischer, IEEE T. Appl. Supercon **22**, 4001505 (2012).
 [3] P. Schnizer, B. Schnizer, P. Akishin, and E. Fischer,

Nuclear Instruments and Methods in Physics Research Section A: Accelerators, Spectrometers, Detectors and Associated Equipment **607**, 505 (2009).

- [4] P. Moon and D. E. Spencer, *Field theory handbook: Including coordinate systems, differential equations and their solutions*. (Springer, 1988).
 [5] L. Brouwer, S. Caspi, D. Robin, and W. Wa, in *Proceed-*

- ings of PAC2013, Pasadena, CA USA* (2013) pp. 907–909.
- [6] P. Schnizer, B. Schnizer, P. Akishin, and E. Fischer, *The International Journal for Computation and Mathematics in Electrical Engineering (COMPEL)* **28** (2009).
- [7] P. Schnizer, B. Schnizer, P. Akishin, and E. Fischer, in *14th International IGTE Symposium* (Institut für Grundlagen und Theorie der Elektrotechnik, Technische Universität Graz, Austria, Graz, 2010).
- [8] A. K. Jain, in *CAS Magnetic Measurement and Alignment*, edited by S. Turner (CERN, 1998) pp. 1–21.
- [9] A. Wolski, in *CERN Accelerator School: Specialised course on Magnets*, Vol. CERN-2010-004, edited by D. Brandt, CERN (CERN, 2010) pp. 1–38, published as CERN Yellow Report <http://cdsweb.cern.ch/record/1158462>.
- [10] S. Gradshteyn and I. Ryzhik, *Table of Integrals, Series and Products*. (Academic Press, 1965).
- [11] V. Marusov, “On relation between elliptic and circular multipoles field representation,” Internal Note (2012).
- [12] B. Auchmann, S. Kurz, and S. Russenschuck, in *18th International Conference on the Computation of Electromagnetic Fields 2011 (COMPUMAG 2011)* (2011) pp. 281–283.
- [13] L. Lewin, D. Chang, and E. F. Kuester, *Electromagnetic Waves and Curved Structures*, Vol. 2 (IEE Electromagnetic wave series, 1977).
- [14] W. D. D’haeseleer, W. N. G. Hitchon, J. D. Callen, and J.-L. Shohet, *Flux coordinates and magnetic field structure* (Springer, 1990).
- [15] B. Seiwald, *On Magnetic Fields and MHD Equilibria in Stellarators*, Ph.D. thesis, Technische Universität Graz (2007).
- [16] SymPy Development Team, *SymPy: Python library for symbolic mathematics* (2013).
- [17] A. K. Jain, in *CAS Magnetic Measurement and Alignment*, edited by S. Turner (CERN, 1998) pp. 175–217.
- [18] W. Davies, *Nuclear Instruments and Methods in Physics Research Section A: Accelerators, Spectrometers, Detectors and Associated Equipment* **311**, 399 (1992).
- [19] P. Schnizer, E. Fischer, P. Akishin, J. P. Meier, A. Mierau, and A. Bleile, in *Proceedings of IPAC2014, Dresden, Germany* (2014).
- [20] E. Fischer, P. Schnizer, A. Mierau, P. Akishin, and J. P. Meier, in *Proceedings of IPAC2014, Dresden, Germany* (2014).
- [21] E. Fischer, P. Schnizer, P. Akishin, R. Kurnyshov, A. Mierau, B. Schnizer, and P. Shcherbakov, in *PAC 09, Vancouver 2009* (2009).
- [22] P. Schnizer, E. Fischer, H. Kiesewetter, F. Klos, T. Knapp, T. Mack, A. Mierau, and B. Schnizer, *IEEE T. Appl. Supercon.* **20**, 1977 (2010).
- [23] G. Moritz, F. Klos, B. Langenbeck, Q. Youlun, and K. Zweig, *Magnetics*, *IEEE Transactions on* **24**, 942 (1988).
- [24] C. Muehle, B. Langenbeck, A. Kalimov, F. Klos, G. Moritz, and B. Schlitt, *Applied Superconductivity*, *IEEE Transactions on* **14**, 461 (2004).
- [25] C. Priano, G. Bazzano, D. Bianculli, E. Bressi, I. De Cesaris, L. Vuffray, M. Pullia, M. Buzio, R. Chritin, D. Cornuet, J. Dutour, E. Froidefond, and C. Sanelli, in *Proceedings of IPAC10, Kyoto, Japan* (2010) pp. 280–282.
- [26] O. Brüning, P. Collier, P. Lebrun, S. Myers, R. Ostojic, J. Poole, and P. Proudlock, *LHC Design Report* (CERN, Geneva, 2004).
- [27] E. Fischer, P. Schnizer, A. Akishin, R. Kurnyshov, A. Mierau, B. Schnizer, S. Y. Shim, and P. Shcherbakov, *IEEE T. Appl. Supercon.* **20**, 218 (2010).
- [28] “FAIR - Facility for Antiprotons and Ion Research, Technical Design Report, Synchrotron SIS100,” (2008).
- [29] H. Khodzhbagiyani, P. Akishin, A. Bychkov, A. Donyagin, A. Galimov, O. Kozlov, G. Kuznetsov, I. Meshkov, V. Mikhaylov, E. Muravieva, P. Nikitaev, A. Shabunov, A. Smirnov, A. Starikov, and G. Trubnikov, in *Proceedings of RUPAC2012, Saint-Petersburg, Russia* (2012) pp. 149–151.
- [30] H. G. Khodzhbagiyani *et al.*, *IEEE T. Appl. Supercon* **21**, 1795 (2011).